DEPARTMENT OF THE INTERIOR

U. S. GEOLOGICAL SURVEY

APPLICATION OF NONLINEAR DYNAMICS TO THE HISTORY OF SEISMIC TREMOR AT KILAUEA VOLCANO, HAWAII

by

Herbert R. Shaw[1]
and
Bernard Chouet[1]

Open-File Report 88-539

[1] U.S. Geological Survey, Menlo Park, CA 94025

UNITED STATES DEPARTMENT OF THE INTERIOR
DONALD PAUL HODEL, Secretary
GEOLOGICAL SURVEY
Dallas L. Peck, Director

For additional information write to:

U.S. Geological Survey
IGP Branch, Room 2280 MS 910
345 Middlefield Raod
Menlo Park, CA 94025

Copies of this report can be purchased from:
Books and Open-File Reports Section
U.S. Geological Survey
Box 25425, Federal Center
Denver, CO 80225
Call (303) 236-7476

TABLE OF CONTENTS

LIST OF FIGURES

ABSTRACT

A 22-year record of seismic tremor obtained by the Hawaiian Volcano Observatory for regions below Kilauea, Mauna Loa, and Loihi volcanoes is analyzed as a system of coupled nonlinear oscillators that has a range of natural and forcing frequencies. Time series are displayed for episode durations, onset intervals, and rates of deep (30–60 km) and intermediate-depth (5–15 km) tremor; locations are determined from correlations with long-period earthquakes. The interval 15–30 km is called the 'quiet zone' because relatively few seismic events of $M \geq 1$ have been located there during this history. Individual tremor episodes range from about 1 to 100 minutes, with few exceptions. Tremor rates (durations divided by onset intervals) demonstrate intermittency, with transient bursts lasting the order of a day to quiescent intermissions lasting months. Cumulative durations over 22 years are 1.60×10^4 min for deep tremor and 0.94×10^4 min for intermediate-depth tremor; the respective yearly averages are 727 and 427 min yr^{-1}. The mean gradient of the yearly average between 5 and 60 km depth is 21.0 min yr^{-1} km^{-1}. The gradient between 30 and 60 km is 24.2 min yr^{-1} km^{-1} and that between 5 and 15 km depth is 42.7 min yr^{-1} km^{-1}. When 2/3 of the quiet zone is included with the intermediate zone and 1/3 with the deep zone, the depth intervals 5 to 25 and 25 to 60 km have gradients equal to the mean. Regimes of nonlinear oscillation are different in the upper and lower regions at constant average moment rates. The upper region is more intermittent; the average onset interval is 19 days and the maximum intermission is 412 days, compared to 14 and 118 days, respectively, for the lower region. Tremor bursts are intensified and quiescence is prolonged in the upper region, suggesting more discrete nonlinear resonances. Fourier analyses of time series and event sequences have a wide range of frequencies in both regions. Counts of episode durations and onset intervals indicate that the geometry of the time data is multifractal (slopes in log-log plots of counts *vs.* length are variable). Return times (iterations between like event parameters) in phase portraits define partitioning of event probabilities. Clustering of event probabilities is described by a function $f(\alpha)$, where α is a measure of the density of the clustering from the most diffuse to the most concentrated region of the phase portrait. The function $f(\alpha)$ defines a locus in α *vs.* $f(\alpha)$ space called a

singularity spectrum. Values of α for tremor portraits range from about 0.3 to 1.9; these are the limiting singularity strengths at $f(\alpha) = 0$. The value $f(\alpha)_{\max} = 1$ corresponds to the Hausdorff dimension, D_0, of the attractor as a whole. Singularity spectra for the 22-year record of tremor appear to be continuous and resemble theoretical spectra for transitions from mode-locked to chaotic attractors. Results suggest a dynamic model of multiple nonlinear oscillators where tuning analogous to that of the sine circle map is itself tuned by the output of functions related to magma generation and transport and to Cantor-like distributions of crack sets that vary with depth. Equations for fracture-limited transport identify alternative scenarios where: (a) magma supply is entirely measured by the record of tremor durations, and (b) aseismic magma transport is required to satisfy transport parameters. A mean-field analysis describes the properties of forcing functions expressed in terms of relaxation times for magma mobility, domain mass, and trigger force for tremor-related fracture. A forcing frequency of 1 $\sec^{-1}$ correlates with the relaxation time for a hypocentral domain of 1-km radius and trigger force of 10^{14} dynes. Extrapolations to the lengths and onset times of tremor episodes imply hierarchies of increasing domain sizes and fractal distributions of magma concentrations from the scale of a hypocenter to that of the lithospheric plate. The energy source of the mean-field transport correlates with the net force of magma rise and compensating subsidence. A parallel is drawn between the complexity of fracture processes and the complexity of fluid trajectories near the onset of turbulence. We call this class of phenomena the *Critical Golden Mean Nonlinearity* (CGMN) because it describes coupled oscillators tuned to a ratio of forcing and natural frequencies equal to the inverse of the Golden Mean, $(5^{1/2} - 1)/2$ (a universal route to turbulence *via* quasiperiodicity).

INTRODUCTION

The regimes of magma transport responsible for volcanism in Hawaii are characterized by vastly different time scales. In the long term, we have fair knowledge of rate regimes in the Hawaiian Archipelago (Jackson *et al.*, 1972; Shaw, 1973; Moore, 1987; Moore and Campbell, 1987), the Hawaiian Ridge (Jackson *et al.*, 1975), and the Hawaiian–Emperor chain (Shaw *et al.*, 1980; Clague and Dalrymple, 1987), for which the relevant time scales are of the orders of 10^{13} to 10^{15} sec (roughly 1 to 73 m.y.). Also, Kilauea's magma supply budget is documented for time scales of the orders of 10^{6} to 10^{9} sec (roughly 2 weeks to 100 years; see Klein, 1982; Dzurisin *et al.*, 1984; Holcomb, 1987; Shaw, 1987a). In the short term there is extensive documentation of long-period earthquakes and tremor associated with individual pulses of magma injection (Koyanagi *et al.*, 1987; Chouet *et al.*, 1987). The characteristic periods are of the orders of 10^{-1} to 10 sec (0.1 to 10 Hz); tremor episodes have durations of the order of 10^{2} to 10^{4} sec (about 1 to 100 minutes), excluding periods of continuous tremor shallower than 5 km that correlate with rift intrusions and surface eruptions (Koyanagi *et al.*, 1987).

Our knowledge of other temporal regimes of magma transport and details of their geometric expression is poor. A qualitative fracture model was outlined by Shaw (1980), and three-dimensional constraints on injection domains are given by Klein *et al.* (1987), Koyanagi *et al.* (1987), and Ryan (1987), but we have no comprehensive description of intermittent transport from the source of mantle melting to the surface for time scales between those of deep tremor episodes and those of magma supply rates determined from inflation-deflation cycles (Dzurisin *et al.*, 1984).

The above frequency range spans about 16 orders of magnitude, but with huge gaps, and we are largely ignorant of the forcing functions that modulate magmatic regimes (time-dependence of the magmatic source, states of magma pressures and stresses in the asthenosphere, lithosphere, and volcanic edifices, etc.; see review by Decker, 1987). We are not able to map magma concentrations within the volcanic edifice and subvolcanic lithosphere at the present time, or over any window in time, except in terms of stylized models such as those of Eaton and Murata (1960), Shaw (1980), and Ryan (1987). There

is little information on spatial densities of transport trajectories or on the magma flux across an arbitrary section of the transport path. For this information we largely relay on tremor and other transport-related seismic phenomena. In addition to the time scales mentioned, tremor durations and intermittencies relate to oscillatory magma transport and earthquake recurrences (Koyanagi *et al.*, 1987; Shaw and Chouet, 1987; Karpin and Thurber, 1987). Thus, given a complete description of tremor we hope to identify universal processes that characterize the dynamic states of a volcano.

Despite the difficulty in achieving this goal, we are encouraged by some remarkable facts about Hawaiian volcanism: foremost is the fact that the process is intermittent at all scales of time and is characterized by similar ranges of magma volume rates at different scales of time and space (Shaw, 1973; Shaw *et al.*, 1980; Dzurisin *et al.*, 1984; Clague and Dalrymple, 1987; Shaw, 1987a). Self-similarity relates to the fact that spatiotemporal regimes are expressions of rate-limiting fracture mechanisms. Magma transport resembles a percolation process in which domains of fluid-filled fractures migrate as they are transiently created and destroyed according to balances of fluid pressures and local states of stress (Pollard, 1976; Hill, 1977; Shaw, 1980; Chouet, 1981).

Within the ranges of temporal and spatial states outlined, intermittent extensional fracture has sustained magma percolation within a selective bandwidth of rates, creating a swath measuring 6,000 km in length by 300 km in width spanning 73 m.y. in time (Jackson *et al.*, 1972; Jackson and Shaw, 1975; Shaw *et al.*, 1980). This process has generated one of Earth's most conspicuous mountain ranges, comparable in volume to Olympus Mons on Mars. If a special balance between magma supply and stress states had not existed, there might have been either the absence of volcanic expression or basalt floods extending over nebulous areas of the ocean floor (*cf.*, Shaw and Swanson, 1970). The fact that magmatic fracture has been sustained within a bandwidth of frequencies that is spatially focused makes this form of volcanism one of Earth's precisely tuned physical mechanisms, rivaling the precision of sea-floor spreading. These observations are not contingent on special models of Plate Tectonics, however; in fact, at present none of these models explain oscillatory and spatially ordered fracture mechanisms that regulate magma transport. We do not address questions of ultimate cause here, but in our analysis

the source mechanism must be consistent with dynamical processes that give rise to the observed fabric of intermittencies.

Support for the above statements is diverse. Models based on continuous conduits are excluded on grounds of mechanical instability, except under transient or near-surface conditions (see Pollard, 1976). Hypocenters of long-period events and tremor, phenomena characteristic of fluid-filled fractures (Chouet, 1988), are distributed discontinuously over immense volumes of the volcanic edifice and subvolcanic lithosphere (Koyanagi *et al.*, 1987). The net transport of magma to high levels, where magma chambers and conduit flow can modulate patterns of eruptive behavior, is dynamically tuned by the aggregate behavior of fluid-filled fractures. Local rates of magma transport at depth correlate with size distributions and longevities of fractures required to compensate the total magma supply to sites of volcanic accretion.

This paper explores the concept that the history of tremor events below about 5 km provides a basis for linking the time scales of seismic responses of the transport path to time scales of magma supply. Toward this end we focus on techniques that may elucidate relationships between the geometric and dynamic complexities of tremor. We make use of developments in fractal geometry and attractor dynamics as the basis for exploring the properties of time-series data and concepts of clustering by which the tremor process and concomitant mass transport can be expressed. At this stage of our study, spatial detail is implicit in that fractures cannot be mapped one-to-one with chronologies of tremor episodes (specific locations of tremor are not resolved). The spatial structure correlates broadly with long-period events mapped by Koyanagi *et al.* (1987). Mean-field calculations discussed in a concluding section provide constraints on fracture distributions and forcing frequencies that may explain the trigger mechanism as well as the time scales of tremor durations.

The plan of the paper is to first describe a 22-year record of tremor episodes in the form of time series and their general properties. These data are used to construct phase portraits, fractal plots of time scales, and Fourier spectra. The structures of attractor basins in the phase portraits are explored by deriving partition functions for recurrence frequencies of the tremor time scales (and implicitly of magma transport pulses). These

partition functions are then expressed in the form of multifractal singularity spectra (Halsey *et al.*, 1986). We conclude the paper by discussing the singularity concept in relation to spatiotemporal scales of magma transport and their time-dependent boundary conditions.

TIME SERIES DATA AND GEOMETRY OF ATTRACTORS

In this section we present data that characterize the history of tremor episodes from 1 January 1962 through 31 December 1983. We include the following information: (a) fence diagrams of tremor episode durations and onset intervals *vs.* time and event number, (b) maps and sections of earthquake distributions, including long-period events and depths of tremor episodes, (c) rate diagrams of episode durations divided by onset intervals, (d) phase portraits (return maps) of durations and onset times, (e) logarithmic frequencies of time data (ranges of fractal dimensions), (f) recurrence diagrams of durations and onset intervals of deep tremor compared with periodic and chaotic attractors, (g) histogram of spacings in return maps and period-doubling, (h) Fourier spectra of rates and event sequences.

This survey of the data leads to concepts of singularity analysis, because the measures are nonunique and multidimensional. Universal singularity spectra described in the literature are characteristic of specific regimes of nonlinear dynamic behaviors. A goal of the paper is to compare dimensional states illustrated in the present section with singularity spectra derived in subsequent sections as a basis for describing complex dynamical states. We feel this is important to the elucidation of chaotic attractors in nature. However, as is shown by controversies in the literature concerning the existence of climate attractors and attractors representing brain wave activity, results based on nonlinear dynamics are not unequivocal (*e.g.*, Nicolis and Nicolis, 1984; Grassberger, 1986; Vallis, 1986; Essex *et al.*, 1987; Mayer-Kress and Layne, 1987).

Despite controversies concerning natural attractors, we believe that the difficulties of deducing a proper embedding dimension in phase space diverts attention from more robust implications of attractor dynamics applied to natural processes. In a broad sense, without regard to the exact degrees of freedom, natural attractors are self-evident. The

evolution of a volcano represents a locus of magmatic trajectories. In that sense it is an attractor even though it may not have a unique set of dynamical parameters. An attractor in the restricted sense refers to the trajectories of motion produced by a specific set of N-dimensional parameters of state (Lichtenberg and Lieberman, 1983, Ch. 1, p. 384). A broader context, discussed in Shaw (1987b), refers to systems of attractors and uses the term attractor generically.

Shaw (1987a) argued that Kilauea operates much like a computer as it iterates a natural algorithm representing the logistics of magma supply (Dzurisin *et al.*, 1984). The corresponding attractor structures are defined by the history of states. There are parallels between that viewpoint, a viewpoint expressed by Robert Shaw in an experimental study of the dripping faucet as a model chaotic system (Shaw, 1984), and the viewpoint of this paper.

The catalog of tremor episodes used in our study was provided by R. Koyanagi of the Hawaii Volcano Observatory. The data are shown in Figure 1 for 578 events of deep tremor and 347 events of intermediate-depth tremor; we exclude shallow tremor (events at depths less than 5 km) because we wish to exclude near-surface noise not directly related to fracture mechanisms of magma transport.

Event durations in Figure 1 are plotted against calendar days from 0.00 H, 1 January 1962. Figure 2 shows normalized event durations and onset time intervals for deep and intermediate-depth tremor plotted in numerical sequence. In these plots, durations were truncated at a maximum of 99 minutes. There are three events of much longer duration in the data for intermediate-depth tremor; they are expressed as consecutive events of 99 minutes duration each, plus a remainder. This truncation was done so that the data sets would have about the same normalized scale. Durations up to 99 minutes per episode are expressed as fractions between 0 and 1; onset times are normalized to the largest intervals (117.92 days for deep tremor, and 412.00 days for intermediate-depth tremor). Peak heights of the onset intervals in Figure 2 give a concise picture of the intermittent character of the records shown in Figure 1; the distributions of peaks gives the patterns of longest durations and intermissions.

Depth zones of the tremor data are shown in Figure 3. These regions were used in the tabulation of data because tremor intermittencies differ; the source depths are separated by a 'quiet zone' that is relatively free of long-period events and detectable tremor episodes. The long-period events in Figure 3 demark hypocentral locations of tremor activity between 1972 and 1984 (Koyanagi *et al.*, 1987, Figure 45.27). Exact locations for all events of Figure 1, however, are not known.

Continuous and Discontinuous Time Series

Figures 1 and 2 show that the time series are both intermittent and discontinuous, relative to the seismic detection threshold for tremor (Koyanagi *et al.* , 1987, give thresholds, respectively, of $M = 1$ and $M = 1.5$ for intermediate-depth and deep long-period events). The term intermittency usually refers to continuous time series data in which there are long intervals of small fluctuations (laminar intermissions) separating bursts of high amplitude irregular fluctuations (Mandelbrot, 1974; Manneville and Pomeau, 1979; Manneville, 1980; Pomeau and Manneville, 1980; Hirsch *et al.*, 1982; Procaccia and Schuster, 1983; Bergé *et al.*, 1984, p. 223 *ff.*; Thompson and Stewart, 1986, p. 340 *ff.*). If our data extended to arbitrarily low magnitudes, we could describe tremor intermittency in these terms, but onset intervals are so long compared to episode durations that the time data are point events analogous to the intervals between drops in the dripping faucet experiments by Shaw (1984). It is difficult to use standard constructions of phase portraits and Poincaré sections for such data. We therefore construct phase portraits in the form of maps in which each value of the variable is plotted versus its subsequent value; these are called return maps, expressed by the relation $x_{n+1} = f(x_n)$ (see Shaw, 1984, p. 5; Bergé *et al.*, 1984, p. 70). The return maps for tremor describe the extremal variations of states represented by the sets of durations and onset intervals.

Geometric analysis of attractors generated from time series has become a standard method in nonlinear dynamics (Packard *et al.*, 1980; Fraser and Swinney, 1986; Mayer-Kress and Layne, 1987). A novel aspect of our approach is that time represents the amplitude parameter as well as the chronological sequence. In this respect our data resemble those of Shaw (1984) for the dripping faucet; he discusses return maps and

dimensions (his Appendix 1 considers continuous time). We take the durations and onset phases of the tremor record as the 'amplitudes' of time series given by the numerical sequences in Figure 2. This is justified in the sense that the state of a system can be characterized by any 'observable' (the parameter of state); an example is the use of isotope ratios in the study of climate attractors (see Grassberger, 1986). Time in the present context is a measure of physical states that characterize the trigger mechanism for the onset of tremor and the states of pressure and stress that sustain magma flow over the timespan of a tremor episode.

In the restricted sense, a phase portrait is a plot of a variable against its time derivative (the classic example being position *vs.* velocity), and an attractor is a characteristic orbit or set of orbits in the phase plot (*e.g.*, Lichtenberg and Lieberman, 1983; Thompson and Stewart, 1986; Moon, 1987). More generally, phase portraits represent values of a variable measured at different times (Poincaré maps are plots of the variable made at constant time intervals and return maps are plots of the sequence of x_n where the time intervals are characteristic of the process). Continuous time series usually involve smoothing. The present data can be made continuous, but not differentiable, by expressing them as rate episodes. Rate curves generated from Figure 1 are shown in Figure 4.

For smoothed data, Poincaré maps of arbitrary dimensionality can be built up from readings at integer multiples of a constant delay time (each axis of the phase space represents one of the integer multiples of the sampling delay time). A Poincaré section is any plane through the phase space on which the piercing points of the parameter trajectories are plotted. Although such plots represent readings at constant time intervals, the time between points in Poincaré sections typically are not constant (Bergé *et al.*, 1984, p. 65 *ff.*). Examples of Poincaré portraits and Poincaré sections of a convection experiment are shown in Figure 5 reproduced from Brandstätter *et al.* (1983). The trajectories at the left define a low-dimensional attractor just prior to breakdown of an interwoven toroidal pattern. In this case, ordered clustering is progressively destroyed by mixing, but the extent to which the pattern is disordered depends on the analysis of the densities of points in phase space (the partition function rather than the macroscopic form is the measure of order).

Questions concerning alternative types of phase portrait for tremor are clarified by the data in Figure 4 (episode rate is analogous to velocity in a standard portrait, and time is analogous to position). Figure 4 defines the average incidence of tremor (minutes per day) as if it were continuous between onset times. Each value is an episode duration divided by the onset interval between that event and the next one; the first onset time is measured from the beginning of the first episode (values would be changed if we divided by the preceding interval, but the ranges would be the same). We could sample Figure 4 conventionally at equal intervals of time, but that would give a distorted picture because the long intervals dominate the readings. Return maps record all of the peaks in Figures 1 and 2.

If we interpret Figure 4 according to the relationship between the tremor mechanism and magma transport envisioned in studies by Chouet (1981) and Aki and Koyanagi (1981), then the amplitude is analogous to transport rate. Comparing the curves for deep and intermediate-depth rates, it is seen that there are differences in the timing of transport in the two depth zones. There are either zones of seismically undetected magma storage in these regions, or there are components of transport not documented by the tremor mechanism. Figure 4 underscores our need for a better understanding of the temporal scaling of the tremor process. We return to these problems in the concluding discussion.

The rate steps in Figure 4 could be smoothed by assuming that they follow the trend of some function of magma flow rate. This seems inadvisable at this stage of analysis, and we adhere to direct representation rather than attempt to construct Poincaré plots even though it is possible to do so. An algorithm by Fraser and Swinney (1986), used in other studies to guide choices of delay time, illustrates the sampling problem. They found that the best time delay is one that minimizes the so-called "mutual information content" of the time series. For time delays short enough to represent most of the variation in Figure 4, there is so much redundancy (long intervals of constant probability) that a minimum is not well defined (*cf.*, Mayer-Kress and Layne, 1987). More importantly, essential information related to short time intervals is lost.

Use of event sequences in Figure 2 avoids loss of information. This assumes that there is no noise in the data of the type Fraser and Swinney (1986) attempt to minimize

(short-term fluctuations in continuous time data often represent extraneous noise). Each event is assumed to be real and to represent the changes we wish to interpret. The use of event sequences effectively compresses the longest time intervals of Figure 4 and expands the shortest time intervals. The spacing between points in the data sequence thus is not constant in time.

Phase Portraits and Fractal Properties of Attractors

Return maps constructed from the event sequences displayed in Figure 2 are shown in Figure 6. They illustrate densities with which similar states are repeated over the sampling history. This information, and the number of steps required to return to the same vicinity (the *recurrence time* in phase space), are the structures we study in later sections. Figure 6 represents the composite of all attractor structures that describe the tremor process, relative to the detection threshold and total length of record. Within these attractor basins there is a great deal of structural detail represented by the densities of recurrences of like states. The notion of attractor basins is analogous to drainage basins in hydrology, where the fine structure represents stream networks and time dependences of flow rates. We note again that our usage is generic compared to formal definitions of attractors and attractor basins (Lichtenberg and Lieberman, 1983).

The fractal character of phase portraits can be explored in many ways. A typical approach for Poincaré plots is illustrated by studies of climate attractors (Nicolis and Nicolis, 1984; Grassberger, 1986; Esses *et al.*, 1987) and brain wave attractors (Mayer-Kress and Layne, 1987). The object is to show the relationship between a correlation dimension (Grassberger and Procaccia, 1983) and an embedding dimension (Nicolis and Nicolis, 1984) of the attractor. If the correlation dimension becomes independent of the order of the time delay used in the construction, then it is assumed to characterize the degrees of freedom needed to define the attractor.

This method is not readily applicable to our return maps, for reasons given above. Also, the degrees of freedom required to calculate the form of a particular attractor is not definitive for systems of attractors. Simple systems can be associated with multi-dimensional attractors, while complex systems can be characterized by low-dimensional

attractors. Lorenz (1962, 1964, 1979) demonstrated that one-parameter systems can generate attractors of unlimited complexity, and it was shown by Shaw (1981) that a quadratic equation can produce information at the same rate as a random number string (e.g., as the pseudorandom reference state of Nicolis and Nicolis, 1984, Figure 5). We defer the issue of proper dimensions to our discussion of singularity spectra.

The average fractal properties of the data can be illustrated by plotting the frequencies of observations, as in the determination of the fractal dimension of a set of statistically self-similar length scales. The fractal dimension D (typically non-integer) is expressed by the relation $N \sim l^{-D}$, where l is a measure of size (yardstick), and N is the number of objects of size equal to or greater than l (see Mandelbrot, 1982). This general definition of fractal dimension is often called the Hausdorff dimension. We test this relationship by plotting the data of Figures 1 and 2 logarithmically in Figure 7. These plots indicate that there is no unique fractal dimension, with the possible exception of Figure 7c (intermediate-depth durations). Clustering of dimensions is suggested by short intervals of constant slope; the solid lines are based on incremental data, reflecting the variability of slopes of the cumulative curves (open circles). Figure 7 shows that the four sets of data have similar statistical properties. That is, the relatively long time scales of onset intervals (typically days to months) resemble the relatively short time scales of tremor episodes (typically minutes to an hour); the ratios of time are roughly similar (min : day and hour : month $\approx 10^3$). This hints that the onset intervals and episode durations may be multifractally self-similar and dynamically correlated (*cf.*, Mandelbrot, 1974).

Tests of Periodicity

Some tests of self-similarity and periodicity in the time series data are shown in Figures 8 through 10. Figures 8 and 9 examine particular suites of periodic states, and Figure 10 gives results of Fourier analyses.

Patterns of divergences and(or) convergences in the return maps of Figure 6 are shown in Figure 8. Figure 8*a* and 8*b* show plots of the expression $\sum_0^N \Delta x = \sum_0^N (x_{n+1} - x_n)$ calculated from the deep tremor data of Figure 6. Figures $8c - f$ show similar summations performed on the logistic equation $x_{n+1} = 4\lambda x_n(1 - x_n)$ (*e.g.*, May, 1976; Feigenbaum,

1978, 1979, 1980) for four values of λ between 0.880 and 0.999. For continuous data, slopes of trajectories in phase space would be determined and the logarithms of their absolute values summed. This provides a Liapunov exponent which measures the rate of divergence from periodic orbits (Shaw, 1981, pp. 88 and 91; Moon, 1987, p. 193). Here we can only test divergences of the discrete states represented by the above summations. Thus, if the phase states progressively shift to larger and larger values, the sum is positive and increasing; if these states shift to smaller values, the sum decreases. The deep tremor data show neither trend, even though they oscillate irregularly. The synthetics of Figure 8*c* show that when return orbits are periodic the sums and ranges repeat at identical positions in the cycle. In the chaotic regime several patterns are possible: (1) nonperiodic cycles (Fig. 8*f*), (2) periodic bands (Figs. 8*d*, *e*), and (3) intermittency (Figs. 8*d*, *e*, *f*). In comparison to these synthetic data, the tremor data have many scales of intermittency.

Even though the tremor data appear to be nonperiodic (Figs. 8*a*, *b*) we cannot tell by inspection whether or not there are components analogous to the periodic bands displayed in Figure 8*d*. As one test of the possibility that there are hidden periodic components of this type in our data we performed a statistical analysis for period-doubling in Figure 9. Period-doubling intervals occur in the experimental data of many nonlinear systems (*e.g.*, Gollub and Benson, 1980; Guevara *et al.*, 1981; Testa *et al.*, 1982; Jeffries, 1985) and are ubiquitous in the chaotic regimes of computer studies (*e.g.*, Shaw, 1987*b*).

Period-doubling in phase portraits shows up as sets of trajectories that repeat themselves every 2^n cycles (where n is an integer) as a tuning parameter is varied (*e.g.*, λ of the logistic equation in Fig. 8). With each generation, as n increases, the trajectories of x in the phase portrait are packed in more densely than in the old generation, and this occurs over narrower and narrower ranges of the tuning parameter (May, 1976; Feigenbaum, 1978, 1980). In other words, the distance between trajectories of a given set is ν times smaller than the distance between the parent trajectories (see bifurcation tree in Fig. 9*C*).

We call ν the packing ratio defined by $\nu = \bar{d}_n / \bar{d}_{n+1}$, where $\bar{d}_n$ is the average spacing between trajectories of the parent set and $\bar{d}_{n+1}$ is the average spacing between trajectories of the period-doubled set (Fig. 9*C*). Feigenbaum (1978) demonstrated that $\nu = 2.5029\ldots$ is a universal constant for quadratic functions. Because we cannot identify specific pairs of

trajectories in our return maps of deep tremor durations (Fig. 6*A*), we can only measure average distances between selected subsets of trajectories. But, if we assume that the return maps are analogous to maps obtained by variable tuning of λ in the logistic equation, then a histogram of counts of $\bar{d}$ will be dominated by bifurcations of low degree (see variation of $\bar{d}$ *vs.* λ in Fig. 9*C*).

In Figure 9*A* we count the numbers of trajectories within a given increment of duration x in the return map and assume that the peaks of the histogram represent a hierarchy of period 2^n with n increasing as the number of counts decreases. Thus, at a given count level (*e.g.*, at count level 20 in Fig. 9*A*) we assume that $\bar{d}$ is represented by the average spacing and divide the total range of x at that level by the number of gaps between the bins intersected. We then assume that the number of bins N is an approximation for 2^n and plot $\log \bar{d}$ *vs.* $\log N$ in Figure 9*B* compared with the same plot obtained for the synthetic period-doubling set in Figure 9*C*.

The similarity of slopes in Figure 9*B* suggests that packing densities of the trajectories of deep tremor durations mimic to some extent those of period-doubling attractors (they differ in detail because N does not correspond exactly to the sequence 2^n and ratios of spacings at large N are not resolved). This conclusion is qualified by the fact that if there is roll-off in the counts of small durations because of threshold effects, then period-doubling could be an artifact of sampling (we return to this point in the discussion of singularity spectra).

Fourier analyses of tremor data in Figures 4 and 8 are shown in Figure 10. No unique periodicities are found (except for a low-frequency peak at 188 days in the deep tremor rates), and the results confirm other indications of statistically complex frequency spectra. If special frequencies exist they are so numerous as to be unresolvable by Fourier analysis. This does not necessarily indicate randomness, because it is shown in other studies that the frequency content of low-dimensional attractors in the vicinity of transitions between mode-locked resonances and chaos can be very great (Fein *et al.*, 1985). If the period-doubling suggested in Figure 9*B* does indeed exist, it is lost in the spectral structure of Figure 10.

The ensemble of tests described so far are inconclusive as to a full description of the attractor object or objects under study. If we had prior information on characteristic frequencies, we could apply tests for coefficients of frequency mixing in Figure 10 (*e.g.*, Gollub and Benson, 1980). In the absence of such knowledge we need better methods for detailed description of the structure of the time series data. The approaches exemplified by tests for general recurrence frequencies (Fig. 7) and period-doubling frequencies (Fig. 9) are made more precise in the next section.

PARTITIONING AND SCALE RELATIONS FOR RECURRENCE TIMES ON AN ATTRACTOR

In this section we develop the concept of singularity spectra as a means to describe the structure of attractors. We first address the mathematical framework for scaling of phase portraits and follow with a description of the partition function required for evaluation of the singularity spectra. The information needed to characterize the dynamic geometry of systems that sample many different scales of length and(or) time is the distribution of states in phase space. Loci of repetition identify basins of attraction, but we do not know how many regimes and types of bifurcation states may be present. Repetition is measured both by the densities of points and by the number of steps (recurrence times) that occur between like states. For example, a fixed point has infinite density at a given value of state parameter and the number of steps per repetition is one. The recurrence time measures the numerical sequence of events in the phase portraits. In the present case it also represents chronologic time, because events in Figure 2 each have a temporal size or 'amplitude.' Because event times correlate with physical parameters of state, the dynamics is mapped by the recurrence behavior (Packard *et al.*, 1980; Nicolis and Nicolis, 1984).

Clustering on an attractor is reflected by variable recurrence times, and documentation depends on the uncertainty with which a point on the attractor can be identified. Large targets of repetition are hit more often than small ones. This introduces a length scale and a method of quantification. Choosing a circle of fixed diameter as a yardstick, we can count the number of points that hit within a given target circle as well as the number of steps that occur between hits, as shown in Figure 11. Because the latter implies the

former, it is the more general measurement. The concept is simple, but the number of ways to define and count target circles are numerous. We follow a method applied to phase portraits of fluid convection by Jensen *et al.* (1985) (their work confirmed the numerical results of Halsey *et al.* , 1986; see also Gwinn and Westervelt, 1987). These experimental studies demonstrated that the form of the singularity spectrum that characterizes the quasi-periodic transition to chaos in low-dimensional attractors is universal.

The method of enumeration is shown by a few counts in the schematic example of Figure 11. Each point in a phase portrait (Fig. 6) is taken as a target center, and the number of steps occurring between that point and the next point that falls within the circle is computed as a function of circle diameter (we later use normalized diameters from 0.01 to 0.8). Permutations of the measurements for different targets generate massive amounts of data. For one of the sets of deep tremor data there are about 600 targets each of which defines a suite of recurrence times for a suite of diameters. By comparison, the analysis of convection patterns by Jensen *et al.* (1985) had 2500 data points (temperature readings at equal intervals of time given by the period of forcing).

Targets (Fig. 11) in the tremor portraits were divided into 60 diameters for each of the data points. Counts of recurrence times vary with target diameter and with location. We estimate that there were 10^5 recurrence times per portrait. The data set of Jensen *et al.* (1985) expressed as a Poincaré section is only four times larger than ours, but the size measured in recurrence counts is much larger. Later we evaluate effects of sample size and the use of return maps on singularity spectra.

Jensen *et al.* (1985) found that in order to treat large quantities of numerical data smoothing is unavoidable (there are too many permutations to see trends in raw counts). Before we describe this smoothing, we give quantitative relationships between length scales, characteristic exponents, and partition functions, following Halsey *et al.* (1986).

Mathematical Relations for Scaling of Phase Space

The attractor is our geometric object, and each visit of its trajectories to a region of specified size is a recurrence event. We divide the object into a number of pieces labeled by an index i that runs from one up to an arbitrary number, N, as in Figure 11. The size

of the i^{th} piece is ℓ_i, and the event occurring on it (each hit in Figure 11) is identified with a quantity, M_i; units of M_i depend on what is being measured (it could be temperature, velocity, tremor duration, etc.). The time series of Figures 1 and 2 (and portraits of Figure 6) are assumed to define all of the events in the tremor record, ignoring thresholds and the finite length of the record. We associate the meaning of M_i with the probability that a reading occurs within the i^{th} piece.

These sequences define the form of the attractor in a phase space of d dimensions, where d is the number of Euclidean dimensions. Although $d = 2$ for graphs in Figure 6, the data are plotted in terms of a single parameter of state (*e.g.*, they could be mapped onto a circle of dimension $d = 1$ by taking normalized values as fractions of the circle; we later compare our results with singularity spectra based on the circle map).

A singularity spectrum based on recurrence times in an assumed geometry is a measure of the existence of an attractor within that framework. In other words, this technique allows one to define the skeletal characteristics of the attractor and is reminiscent of X-ray analysis of complex crystals. Because we include all events in the phase space, the spectrum (if it exists) will be the most faithful description of the data, even if not the most precise. Averaging based on Figure 4, for example, could improve precision, but we would lose information about the dynamical structure.

Expressed in terms of the d-dimensional space, the densities of a quantity imagined to fill the space is normalized by ℓ^d. The ordinary spatial density is identified by:

$$\rho(\ell) \sim \frac{1}{\ell^d} \quad . \tag{1}$$

Trajectories of events that produce the form of an attractor do not fill the entire d-space. We then say that the trajectories lie on an attractor of dimension D, for $D < d$. If we multiply (1) by ℓ^d and divide by ℓ^D, then the density expressed relative to D is proportional to ℓ^{-D}, the definition of fractal dimension, D.

Densities of events according to Eq. (1) depend on counts (N_i) of how often the time series visits target pieces of specified sizes (ℓ_i). But our data only tell us how often a target within a spectrum of targets is visited (Figure 11). There is no information for portions of

d-dimensional space not visited at a given target size. Average densities from Eq. (1) are not diagnostic of densities on the attractor. The information available is the number N_i of visits to a specified target relative to the total events on the attractor, N. The quantity N_i/N estimates the probability $p_i = \lim_{N\to\infty}(N_i/N)$. This is the concentration (strength of focus) of events in fractal phase space.

If the distribution were uniform over the phase space, and the dimension of the attractor were $D_{\text{const.}} \leq d$, the frequency of visits, N_i, would be proportional to ℓ^D (*e.g.*, if $D = d$, uniform N_i is proportional to ℓ for $d = 1$, to ℓ^2 for $d = 2$, and to ℓ^3 for $d = 3$). When there is clustering, exponents of ℓ are variable and generally unknown; if clustering is discrete, there are discrete exponents (analogous to indices of critical phenomena), and if clustering is interwoven, there are continuous sets of exponents.

We define a function α as a variable scaling exponent, as follows:

$$p_i \sim \ell_i^{\alpha} \quad , \tag{2}$$

where $p_i \approx N_i/N$ is the probability of N_i recurrences among the total set of N recurrences occurring within pieces characterized by length ℓ_i.

This definition of α resembles a fractal dimension, but it is usually termed the *singularity strength*. Inverting Eq. (2), $1/p_i \sim \ell_i^{-\alpha}$, we see that α is a fractal dimension of a set of $1/p_i$ objects of sizes ℓ_i. Because $1/p_i = N/N_i$, the set represents the number of domains of length ℓ_i within which there are N_i recurrences relative to the total set of N recurrences. This number increases with decreasing N_i, and α gives the corresponding fractal dimensions; α is greater for small and rapidly varying N_i (tenuous regions) and smaller for large and slowly varying N_i (concentrated regions).

There is no restriction on clustering of self-similar subsets, nor on the possible values of α. If there were a portion of an attractor where N_i varied by four orders of magnitude while ℓ_i varied by one order of magnitude, the proportionality is $N_i \sim \ell_i^4$ in that vicinity even if the Hausdorff dimension is small. The problem is to find a way to characterize the distribution of events in terms of α, whether it takes on discrete values or it varies over

a spectrum of singularities. In the latter case clustering is so interwoven that individual domains cannot be isolated in the fabric of singularities (see Fig. 5).

In order to complete the description we need a function for the variation of α. Therefore, the frequency relation is expanded to bring out the fine structure of the density variations. Another scaling exponent, q, is introduced as an operator that generates arbitrary enlargements and(or) reductions of the probability distributions. This represents an expansion of the event counts in the phase portrait, permitting us to zoom in on different portions of the attractor. Expressed in terms of the event frequency, N_i^q, large counts are made arbitrarily larger or smaller while small counts are not greatly affected, so the scaling of frequencies is fanned out over an arbitrary range.

Recurrence times fan out under expansion, so α can also be represented by how p_i varies with q. The recurrence time, symbolized m_i, is taken to represent the inverse of the probability, $m_i = 1/p_i$. Slopes (τ) in a diagram of $\log m_i$ (expanded for different q-values) *vs.* $\log \ell_i$ represent the magnifying factors for domains of differing singularity strengths. To make the parallel precise, Eq. (2) is rewritten in the form:

$$p_i^q \sim \ell_i^{\alpha q} \quad . \tag{3}$$

We can now generate a function, $f(\alpha)$ by using the same logic that was applied to the distributions of event frequencies. The function sought represents variations of α over different domain sizes, ℓ_i, and can be expressed in terms of $n(\alpha, \ell)$, given by the number of times α takes on a value between α and $\alpha + d\alpha$ as a function of ℓ. The increment in α times the local event density characterized by α defines $n(\alpha, \ell)$ in terms of another function of ℓ:

$$n(\alpha, \ell) = d\alpha \rho(\alpha) \ell^{-f(\alpha)} \quad , \tag{4}$$

where $\rho(\alpha)$ represents N_i normalized by ℓ^α, and $f(\alpha)$ is a function that scales α to the length-scale ℓ.

If α varies continuously over the attractor, then $f(\alpha)$ is a differentiable fractal function. At $f(\alpha) = 0$, the scaling is invariant (constant α). Typically there are two such limits, one

for the most rarefied region of the attractor ($\alpha_{\max}$) and the other for the most concentrated region ($\alpha_{\min}$). Between these limits $f(\alpha)$ reaches a maximum that coincides with the fractal dimension of the attractor as a whole (the Hausdorff dimension, D_0).

The Partition Function

In order to evaluate α and $f(\alpha)$, we need a partition function Γ for the complete set S_i of measures p_i. The derivation is given in Halsey *et al.* (1986) and in Procaccia (1986). The partition equation is defined by

$$\Gamma(q,\tau,S_i,\ell) = \sum_{i=1}^{N} \frac{p_i^q}{\ell_i^\tau} \quad , \tag{5}$$

where summations are over all members of the set, and τ is defined by

$$\tau = \lim_{\ell \to 0} \frac{\log \Sigma p_i^q(\ell)}{\log \ell} \quad . \tag{6}$$

It is shown by Halsey *et al.* (1986, p. 1142 *ff.*) that, for large N, Eq. (5) is of order unity, and Eq. (6) shows that τ is the slope in logarithmic plots of expanded probability *vs.* ℓ at constant q; τ is the magnifying factor described above.

The probability is expressed in terms of α and $f(\alpha)$ by combining relations (3) and (4) and integrating to give the function

$$\sum p_i^q(\ell) = \int d\alpha \rho(\alpha) \ell^{-f(\alpha)} \cdot \ell^{q\alpha} \quad . \tag{7}$$

In the limit $\ell = 0$, Eq. (7) is dominated by the value of α that minimizes $(q\alpha - f(\alpha))$. Taking logarithms and dividing by $\log \ell$, it is seen that the net exponent $(q\alpha - f(\alpha))$ can be substituted for the right side of Eq. (6), yielding

$$\tau = [q\alpha(q) - f(\alpha(q))] \quad , \tag{8}$$

and, by partial differentiation,

$$\alpha(q) = \frac{d\tau}{dq} \quad . \tag{9}$$

Given values of q and τ, $\alpha(q)$ is found from Eq. (9) and $f(\alpha)$ from Eq. (8).

Evaluation of α and $f(\alpha)$

In order to obtain (q, τ) sets from times series data, recurrence times from Figure 6 are used to evaluate probabilities, following Jensen *et al.* (1985). Probabilities are expanded over selected ranges of q to give corresponding values of τ as graphical slopes over specified ranges of $\log \ell$. We then evaluate α and $f(\alpha)$ usings Eqs. (8) and (9).

Prior to expansion, we associate the recurrence time, m_i, with the reciprocal of the probability, p_i (Jensen *et al.*, 1985):

$$m_i = \frac{1}{p_i} \quad . \tag{10}$$

Therefore, from Eq. (2) we have

$$m_i = \ell_i^{-\alpha_i(\ell)} \quad , \tag{11a}$$

or

$$\alpha_i(\ell) = \frac{-\log m_i}{\log \ell_i} \quad . \tag{11b}$$

Eq. (11b) represents spot estimates of α prior to expansion, but it does not adequately identify $f(\alpha)$.

To carry out an evaluation, we average the probabilities expressed by the recurrence time in the expanded form (Jensen *et al.*, 1985):

$$\langle p_i(\ell)^{q-1} \rangle = \langle m_i^{1-q} \rangle \quad . \tag{12}$$

where braces indicate that recurrence times are averaged at a fixed value of q and ℓ over all of the points in phase space. This averaging is done for a range of q-values between $-\infty$ and $+\infty$, and for a range of normalized ℓ-values between 0 and 1. Replacing probability summations in Eq. 5 by averages from Eq. (12), the partition function is still of order unity, and τ is given by the slope of $\log \langle m_i^{1-q} \rangle$ *vs.* $\log \ell$. The slopes (τ) are negative for $q < 1$, zero for $q = 1$, and positive for $q > 1$.

The expansion of recurrence times described by Eq. 12 satisfies two goals: (1) It places the phase data in a form consistent with generalized dimensions of a partition function (Hentschel and Procaccia, 1983; Grassberger and Procaccia, 1983). (2) It smooths inconsistencies of raw values of $\log m_i$ *vs.* $\log \ell_i$ by averaging $\langle m_i^{1-q} \rangle$ over many combinations of q and ℓ.

Hentschel and Procaccia (1983) emphasized that a fractal object is not completely characterized by the Hausdorff dimension (*cf.*, Mandelbrot, 1986). They designated families of fractal dimensions by the symbol D_q, where q is unlimited. Integer values of q correspond to other definitions of fractal dimensions: *e.g.*, the values $q = 0$, $q = 1$, and $q = 2$ correspond, respectively, to the Hausdorff dimension, the information dimension, and the correlation dimension, symbolized D_0, D_1, and D_2. It was shown that $D_2 \leq D_1 \leq D_0$ for the classes of fractals considered by Hentschel and Procaccia (1983, p. 436; *cf.*, Grassberger and Procaccia, 1983). These values are often nearly equal and represent three points on the singularity spectrum clustered near the maximum value of the spectrum, D_0. Thus, a general evaluation of D_q clarifies the issue of correlation dimension (D_2) previously discussed. Halsey *et al.* (1986) described ways to express D_q in terms of variable scaling dimensions and coined the term *singularity spectra* of fractal measures. They showed that $\tau = (q-1)D_q$, which approaches asymptotic limits ($D_{+\infty}$, $D_{-\infty}$) at $q = \pm\infty$; near these limits τ is almost proportional to q because D_q is nearly constant beyond $q = \pm 40$.

In practice, m-values were determined as in Figure 11 over a range of target diameters (ℓ-values), taking each one of the points in the phase portrait in turn as a target center. The number of steps between each hit represents a value of m_i, and each point in the phase portrait could theoretically represent anywhere from zero to an infinite number of hits in that vicinity, depending on target size. Every m_i, at given ℓ, is raised to the power q, and each set is averaged at that value of ℓ and q over all target points, providing a list indexed by q and ℓ.

We chose 60 increments of q at values between -7 and $+12$ to represent the range of variation in α-sets, compared with the range -40 to $+40$ in Halsey *et al.* (1986, Figures 13 and 14). Increments of q ranged from ± 0.1 near $q = 0$, to ± 1 at the largest values. Although the asymptotes of D_q (invariant limits of α) are not reached even at $q = \pm 40$,

much of the variation of $f(\alpha)$ *vs.* α occurs within $q = \pm 10$. We did not investigate larger absolute values of q because of propagation of errors and limitations on computer time.

Logarithmic plots of $\langle m_i^{1-q} \rangle$ *vs.* normalized target diameters, ℓ, at constant values of q are given in Figure 12 for each of four sets of tremor data. In each case there were 64 values of ℓ at equal increments between 0.01 and 0.80 within the normalized interval 0 to 1. These plots are the primary data for the fractal properties of the phase portraits.

Figure 12 gives us a number of possible regression fits of $\log \langle m_i^{1-q} \rangle$ *vs.* $\log \ell$ so that the estimates of τ are not uniquely fixed. This is expected for limited data sets (*cf.*, Gwinn and Westervelt, 1987). Instead of relying on such fits we take a more robust graphical approach based on Eqs. (6) and (12), combined with Eqs. (8) and (9), that allows us to simultaneously evaluate τ, α and $f(\alpha)$. This is described in Figure 13.

Figure 13*A* shows that when we evaluate an apparent value of τ (τ_a) as slopes defined by the ratio of $\log\langle m^{1-q} \rangle / \log \ell$, the range of values is smaller than the range of partial regression slopes in Figure 12. The effect is similar to forcing the regression through the origin $\log\langle m^{1-q} \rangle = 0$, $\log \ell = 0$. Although this is not rigorously equivalent to Eq. 6, we found by testing many combinations of $\log\langle m^{1-q} \rangle$ and $\log \ell$ that results are more systematic on this basis, particularly for ℓ not much greater than 0.1 nor much smaller than 0.01. Given sets of τ_a, we approximate α from Eq. 9 in the form $\alpha \simeq \Delta\tau_a / \Delta q$ for chosen values of ℓ. This defines the product $q\alpha$ in Eq. 8 for each set. Eq. 8 also shows that $f(\alpha) = q\alpha - \tau$. Therefore, we plot τ_a and $q\alpha$ against q on the same coordinates. Differences between these values establish ranges of $f(\alpha)$ at each value of q. Examples are shown in Figure 13*B* for three values of $\log \ell$ (-1.0, -1.4, and -2.0) for a small data sample.

This method is approximate but it is numerically direct and it identifies compatible ranges of τ, α, and $f(\alpha)$. In most cases we find that relationships are most consistent for values near $q = 0 \pm 6$. Outside this range, plots of τ *vs.* $q\alpha$ may cross, indicating negative $f(\alpha)$, which is not physically meaningful. The graphical method of Figure 13 is used to test the crossover effect *vis a vis* variations of $\log\langle m^{1-q} \rangle$, $\log \ell$, and τ_a. It also illustrates the stability of solutions at $q = 0$, where $f(\alpha) = D_0$, and at nearby values corresponding to D_1 and D_2 (the latter can be evaluated by constructing curves of D_q based on the relation $\tau = (q-1)D_q$, and interpolating for $q = 1$ where the solution is indeterminate). These

relationships are summarized schematically in Figure 13*C*; the dashed curves represent the uniform (random) set where $\alpha = f(\alpha) = 1$. Because $f(\alpha)_{\max} = 1$ for the analyzed data, the dashed curves converge with the stippled envelope at $q = 0$.

SINGULARITY SPECTRA

Given numerical techniques for the characterization of singularity spectra described above, our main task is to apply them to the tremor data and to interpret the results in terms of known geometric structures of attractors and in terms of consistent physical processes. In the present section we give α *vs.* $f(\alpha)$ curves for tremor and compare them with well established singularity spectra obtained for coupled oscillators. These include physical experiments and a simple numerical model of coupled oscillators provided by the sine circle map. The latter has become widely recognized as a useful function for the study of nonlinear dynamic regimes; summaries of its general properties are given by Jensen *et al.* (1984), Fein *et al.* (1985), Bak (1986), and Shaw (1987*b*) (*cf.*, Thompson and Stewart, 1986; Moon, 1987; and Schuster, 1988).

Results for Kilauean Tremor

Relationships summarized in the preceding section were used to determine singularity spectra of α *vs.* $f(\alpha)$ based on Eqs. (8) and (9) and Figures 12 and 13. Because the graphical determination of τ_a is most consistent for $-2 \leq \log \ell \leq -1$, we evaluated τ_a for tremor data in Figure 12 for two values of ℓ, 0.1 and 0.01. Using these two sets of τ_a for the range $-7 \leq q \leq +12$ we obtained the corresponding values of α and $f(\alpha)$ by the method of Figure 13 together with their averages at each value of q. The results are shown in Figure 14.

Reference curves in Figure 14 (solid lines) refer to a special regime of the sine circle map described in the next subsection. Our results can be compared to those of Jensen *et al.* (1985) obtained in a study of the quasi-periodic transition to turbulence in a system of coupled oscillatory convection (the spectrum they analyzed describes a structure analogous to that illustrated in Figure 5 near breakdown). The result for deep tremor durations

(Fig. 14*a*) resembles that of Jensen *et al.* (1985) with regard to $f(\alpha)_{\max} = D_0 \simeq 1$ and $\alpha_{\max} \simeq 1.9$ (most tenuous region of the attractor). Values of $f(\alpha)_{\max}$ are smaller in the other sets of tremor data (Figs. 14*b* – *d*), and $\alpha_{\min}$ is much smaller than those of the reference curve and the singularity spectrum of Jensen *et al.* (1985). Error propagation in our analysis of the tremor data is severe at large and small α compared to their results (see discussion of Fig. 13). The resolution of these spectra is discussed in the next subsection using an artificial data set based on the sine circle map. Physical analogies between the fractal structures of fluid turbulence and of tremor events will be discussed later.

Comparative Study of the Sine Circle Map at the Transition between Quasi-periodicity and Chaos

As a standard of comparison, we analyzed the same number of data points in artificial time series and return maps generated using the sine circle function (see Shenker, 1982; Jensen *et al.* , 1984; Fein *et al.* , 1985; Halsey *et al.* , 1986; Bak, 1986; Shaw, 1987*b*).

The sine circle map is appropriate for the study of the fractal geometry of low-dimensional attractors for several reasons: (1) It is the simplest paradigm for coupled nonlinear oscillators (Bak, 1986; Shaw, 1987b). (2) It demonstrates transitions to chaos *via* quasi-periodicity that resemble the quasi-periodic transition to turbulence in fluids (*e.g.*, Jensen *et al.*, 1985; Fein *et al.*, 1985). (3) It demonstrates power spectra at the critical transition that are self-similar over an infinite range of ordered frequencies (Fein *et al.*, 1985). (4) It illustrates simple to complex clustering of trajectories in phase space and demonstrates several types of singularity spectra (*e.g.*, Halsey *et al.*, 1986). (5) It shows how nonlinear systems are tuned and provides criteria for discrimination between mode-locking and chaos.

Finite difference recursion on the circle is analogous to studies of the quadratic equation of Figure 9, except that the control function is sinusoidal and there is an adjustable phase delay. We write a return function equivalent to $x_{n+1} = f(x_n)$ in terms of an angle θ expressed as a fraction of a revolution on the circle

$$\theta_{n+1} = \theta_n + \Omega + \left(\frac{K}{2\pi}\right) \sin(2\pi\theta_n) \quad , \tag{13}$$

where θ_n is the present value of the angle, θ_{n+1} is the next value calculated from the function, Ω is the bias (or *bare winding number*), and K is the strength of nonlinear coupling.

Numerical recursion is performed by solving for θ_{n+1}, subject to assigned values of Ω, K, and an initial value of θ, and then substituting that value into the function as the next value of θ_n. A transition between a regime of periodic attractors (the regime of mode-locking and quasi-periodicity) and a regime of chaos occurs exactly at $K = 1$. This is the transition from a monotonic control curve to one with a local maximum; that is, there is a cubic inflection in the control curve at $K = 1$, and trajectories of motion at higher values of K are not invertible. The effect of maxima in the control curve is to cause overlap and mixing of the trajectories so that reversibility is destroyed (*e.g.*, Fein *et al.*, 1985). An effect of this folding is that stable windows of integer period occur in the chaotic regime of the circle map just as they do in the chaotic regime of quadratic maps (*e.g.*, Crutchfield *et al.*, 1986, p. 57; Shaw, 1987b, Figure 2). These windows bifurcate in period-doubling sets as K increases at constant Ω, or as Ω varies at constant K (in the latter case, forward and reverse bifurcation sets are characteristic; Shaw (1987b, Figure 2i)).

For $0 < K \leq 1$, attractors may be either mode-locked or quasi-periodic. Mode-locked states are those in which the average angular iteration per cycle in Eq. (13) is a rational fraction. The average angle of nonlinear iteration is called the *winding number* (sometimes the *dressed winding number*), W, defined by:

$$W = \lim_{n \to \infty} \left[\frac{(\Sigma\theta - \theta_0)}{n} \right] \quad , \tag{14}$$

where $\Sigma\theta$ signifies the total angular rotation relative to the initial position θ_0, and n is the total number of iterations. Quasi-periodic trajectories are those for which W is an irrational fraction. In general, W is not simply defined in the chaotic regime.

Using Eq. (13) we generated sets of data which we plotted in the same way as the phase portraits of tremor. In this study, the winding number, W, in Eq. (14) was set at the inverse of the Golden Mean $= (5^{1/2} - 1)/2$, or $W_g = 0.618034 \ldots$. We term this universal condition of coupled nonlinear oscillations the Critical Golden Mean Nonlinearity,

CGMN (Shaw, 1987*b* discusses why this state of tuning may be applicable to periodicities in nature). The CGMN is a powerful idea because it characterizes self-similarity over many scales by a single curve in α *vs.* $f(\alpha)$ space. Self-similarity occurs because W_g can be approximated by a unique series of rational fractions (see Shaw, 1987*b*). In the laboratory, W_g can be arbitrarily set by adjusting a forcing frequency relative to the natural frequency of the system. By trial and error convergence we found that the value of bias, Ω, required to give $W = W_g$ to an accuracy of 10^{-15} is $\Omega = 0.6066 \pm 0.0001$. That is, an irrational value of W occurs over a range of Ω, and it is impossible to give exact correspondances (problems of tuning to the CGMN are discussed in Fein *et al.* , 1985). We studied the range $\Omega = 0.61 \pm 0.01$ and found that spectra of α *vs.* $f(\alpha)$ within this range could not be distinguished on the basis of time series having 600 data points. The expansion of recurrence times for the circle map is shown in Figure 15*A*.

Singularity spectra of α *vs.* $f(\alpha)$ for the circle map with $\Omega = 0.61 \pm 0.01$ are estimated by the dashed curve in Figure 15*B*, compared with the numerical curve of Halsey *et al.* (1986) (solid curve). The locus of points calculated by us is at slightly lower α but has about the same maximum, $f(\alpha) = 1$ (the Hausdorff dimension). Uncertainties evaluated by the method of Figure 13*B* are indicated by the error rectangles. Error bars shown by Jensen *et al.* (1985) for the singularity spectrum determined from convection data (2500 points) are smaller than those in Figure 15*B*, and error bars shown by Gwinn and Westervelt (1987) for an experimental system of about 70,000 data points are smaller than those of Jensen *et al.* (1985). Based on these three data sets, the uncertainty appears to decrease roughly as the 1/4 power of the number of points in a phase portrait.

The form and uncertainties of the singularity spectra for the tremor data (Fig. 14) are similar to those in Figure 15*B*. We note the following features of our tremor analyses relative to the CGMN curve: (1) The spectra for deep tremor roughly resemble the CGMN regime of the circle map (solid curves in Fig. 14) with regard to $f_{\max}$ and $\alpha_{\max}$ for both the durations and onset times. (2) The spectra for intermediate-depth tremor are shifted to lower values of $f_{\max}$ and $\alpha_{\max}$ in both modes. (3) The values of $\alpha_{\min}$ are similar in all the tremor spectra and are roughly half the value of $\alpha_{\min}$ of the CGMN (the latter is theoretically 0.6326..., while $\alpha_{\min}$ for tremor is about 0.3 to 0.4). (4) Convergence of

$q\alpha - \tau$ near $f(\alpha)_{\max}$ in Figures 13*B* and 13*C* suggests that values of D_0, D_1, and D_2 are approximately equal. Arguments summarized below favor the conclusion that uncertainties are partly a result of sample size and partly a result of composite effects.

Examples of Singularity Spectra for Other Objects and for Different Regimes of the Circle Map

As a rule, attractors can be represented by points and(or) continuous curves in α *vs.* $f(\alpha)$ diagrams. Continuity and ranges of dimensions determine the geometric distinctions. Dynamical systems tuned to more than one regime of behavior may show degeneracies and(or) composite effects. A phase portrait generated by the sine circle function (Eq. 13) for conditions where Ω and K take values sometimes in the mode-locked regime and sometimes in the chaotic regime would display composite properties. Period-doubling is an inherent structure of the chaotic regime (see examples in Shaw, 1987*b*).

Examples of different singularity spectra α *vs.* $f(\alpha)$ are shown in Figure 16. Figure 16*A* represents a two-scale Cantor set, Figure 16*B* illustrates a period-doubling set, Figure 16*C* shows mode-locked sets of the sine-circle map, Figure 16*D* represents the critical transition of the circle map (CGMN), Figure 16*E* is a schematic of a truncated singularity spectrum, and Figure 16*F* shows a degenerate set representing the nonsingular background $f(\alpha) = \alpha = 1$ interrupted by singularities of a discrete set with arbitrarily fixed α and $f(\alpha)$; the set plots at two points (1,1) and $(\tilde{\alpha}, \tilde{f})$ in the α *vs.* $f(\alpha)$ diagram. A uniformly random set would plot at a single point $\alpha = f(\alpha) = 1$ (*cf.*, Fig. 13*C*). We are especially interested in how the critical spectrum (Fig. 16*D*) relates to period-doubling (Fig. 16*B*), mode-locking (Fig. 16*C*), and chaotic spectra because this may help explain differences between singularity spectra of tremor and the CGMN reference curves of Figure 14. The chaotic regime does not have a unique singularity spectrum, but period-doubling exists within this regime.

If tuning of the transition between mode-locked, quasi-periodic, and chaotic regimes of coupled oscillators is precise, the singularity spectrum is sharply defined and universal (Fig. 16*D*). We have called it the CGMN condition by analogy with the sine circle map (Fig.15) and with experimental data on oscillatory convection (Fein *et al.*, 1985; Bohr

et al., 1984; Jensen *et al.*, 1984; Jensen *et al.*, 1985) and on current oscillations in tuned semiconductors (Bohr *et al.*, 1984; Gwinn and Westervelt, 1987). A Poincaré section of continuous data would resemble the clustering of points on a closed loop or section through a torus, as in the lefthand diagram of Figure 5, or in Figure 16D (panel b). This is not seen in tremor portraits of Figure 6 because we are dealing with discontinuous sampling of a system of attractors and we cannot view this as a simple manifold such as that for the breakdown of a quasi-periodic route to chaos shown in Figure 5.

Singularity spectra of tremor (*Fig.* 14) resemble the transition between mode-locking and chaos. However, $f(\alpha)_{\max}$ is too low (with the exception of the curve for deep tremor durations, Fig. 14*A*), and $\alpha_{\min}$ is consistently too small. Both effects could be caused by components of period-doubling and(or) mode-locking combined with the CGMN regime (compare Figs. 16*B*, 16*C*, and 16*D*). These admixtures tend to shift α and $f(\alpha)$ to smaller values than those of the CGMN spectrum. Low values of $\alpha_{\min}$ suggest that the regions of most frequent recurrences in phase space (densest part of the attractor) have a flat distribution compared to the CGMN structure (see Eq. 2). However, roll-off related to incomplete sampling of tremor events below the detection threshold might also shift $\alpha_{\min}$ to low values (*cf.*, Fig. 7). Despite these qualifications, the resemblances between singularity spectra for both tremor durations and onset time intervals in Figure 14 favor the idea that the tremor process is generally self-similar over all temporal scales.

PHYSICAL INTERPRETATION OF SINGULARITY SPECTRA FOR KILAUEAN TREMOR

In this section, we address the budget of magma transport under Kilauea volcano from the perspective of the singularity spectra that we have derived for the history of tremor. We interpret the volume domains of tremor sources in relation to sets of discrete fluid-filled fractures. Then, we analyze the relation between the relaxation process of these volume domains and the trigger mechanism for the activation of tremor. We express this relation by a mean-field model of fractal transport and forcing frequencies in which the average magma mobility is defined in terms of the trigger force and compatible relaxation times.

The above indications of composite effects suggest a model of coupled nonlinear oscillators where a tremor-generating mechanism analogous to the circle map is tuned by the output of feedback functions related to magma transport regimes (Shaw, 1987*a*; in press). For these reasons, and others given below, we infer that the dynamics is manifested by Cantor-like distributions of fluid-filled cracks. An example of a singularity spectrum for a spatial distribution modeled as Cantor sets is shown in Figure 16*A*. Accordingly, the singularity strength α would resemble the spatial distributions of inverse probabilities of flow-related tremor events, and $f(\alpha)$ would represent fractal distributions of these sets. By this view, singularity spectra provide signatures by which to compare and classify geometries of fracture systems that characterize mass transfer as functions of magma concentration, fracture geometry, rock strength, fluid pressure, and stress states. A schematic section of the path between the source of magma generation and the surface is shown in Figure 17.

Admittedly, structures in phase portraits of tremor data do not necessarily describe the spatial distributions of magma injection. However, evidence of universalities in singularity spectra for temporal data suggest possible universalities in spatial geometries by analogy with nonlinear periodicities of complex crystalline materials (Bak, 1986). That is, magma transport is envisioned to oscillate in spatial modes consistent with the temporal modes, and magma injection events are imagined to be analogous to particle trajectories in fluid flow near critical self-similarity. If so, the injection plexus is ordered over many scales of length and is sampled in modes departing either toward chaos or toward mode-locking depending on interactions of one or more forcing functions with the natural periods of the system.

The Volume Budget of Fracture-Related Magma Transport

Computer models of vibrating fluid-filled cracks and their radiation fields are described by Chouet (1988). Comparison of these models with the durations of deep and intermediate-depth tremor indicates that more than a single magma-filled fracture must be activated per episode. An enumeration based on an event duration of about 20 sec (Chouet, 1988, Fig. 1) for ongoing tremor lasting of the orders of 1 to 100 minutes implies

that there are of the orders of 3 to 300 activated cracks per tremor episode; 20 seconds is used as a basis for the definition of a reference volume, V_0, that permits us to evaluate the volume budget of magma transport from our counts of tremor episodes. This assumes that a tremor episode is a composite of interacting long-period events, as inferred by Koyanagi *et al.* (1987), Chouet *et al.* (1987) and Chouet (1988). The multiplicity of events, combined with variable viscosity and stiffness, suggest that the acoustic responses of tremor episodes have aspects that resemble the fluttering of a system of reeds or septa within a dendritic ensemble of fluid-filled cracks (*cf.*, Figs. 16*A* and 17*B*).

If we take an average of about 50 fractures per tremor episode within a hypocentral domain with an assumed radius of order 1 km and multiply by the number of episodes in the 22-year record (about 1000 events), we obtain 50,000 fractures (the cumulative duration of the entire record divided by 20 sec gives about 76,000 fractures but we use 50,000 as a reference set). The fractures are distributed in clusters of many sizes between 5 km and at least 60 km depth and within a vertical cylinder of the order of 35 km radius (see Figure 3); this includes volumes between the conduit-like avenues of transport discussed by Koyanagi *et al.* (1987) and Ryan (1987). We do not restrict the enumeration to Kilauea proper because the general system includes transport paths beneath Mauna Loa and Loihi volcanoes, as shown in Figure 3 (if hypocenters of short-period events are included, the radius of influence is larger).

If the 1-km radius is an average, and if tremor episodes do not recur at exactly identical locations, then the cumulative volume of domains is of the order of 10^3 km^3 (average hypocentral volume times number of episodes). This is roughly 10^{-3} times the total cylinder within which hypocenters are distributed down to a source below 60 km; *i.e.*, we have a structure of nested volume domains of variable dimensions: the total hypocentral volume fills a small fraction of the total rock column, and magma-filled fractures fill a small fraction of the hypocentral volume. Although we cannot measure these domains, this is a fractal distribution (the average magma concentration becomes smaller as the size of the domain in which it is evaluated becomes larger; see Mandelbrot, 1982, p. 85).

These estimates exclude fractures that correlate with tremor below the limits of seismic detection, but volumetric estimates will be larger only if the numbers of small-volume

events dominate the statistics (size frequencies of basaltic dike swarms are discussed below). Assuming that each fracture has a characteristic volume that represents an increment of net magma transport in a quasi-steady process, we can estimate the mean volume of a reference fracture from a knowledge of magma supply. We take a supply rate of 0.1 km^3/yr (see Shaw, 1987a, Figure 51.7), giving 2.2 km^3 of magma delivered to sites of eruptions and shallow intrusions over the 22-yr history. We want to know if this volume is consistent with a reference set of 50,000 fractures inferred from the total duration of tremor.

If we assume that these fractures have opened and closed like paired sets of bellows (on average, opening events and closing events balance), and the displaced volume is delivered to the surface, then the average volume per magma injection pulse is $2.2 \times 10^9/50,000 = 4.4 \times 10^4$ m^3, and the equivalent flow rate normalized to 20 sec is about 2×10^3 m^3/sec. A fracture consistent with this volume would have dimensions of about 200 m $\times$ 200 m $\times$ 1 m. These values resemble those inferred by Aki and Koyanagi (1981, p. 7107) and by Chouet (1981, p. 6014) from seismic models of extensional episodes involving paired cracks: their estimates, respectively, were 700 m^3/sec and 929 m^3/sec, giving 1.4×10^4 and 1.9×10^4 m^3 for a magma injection pulse normalized to 20 sec during a composite episode. Fracture dimensions inferred from the above three volume estimates are comparable.

Dike measurements provide additional checks on fracture dimensions. The median value for dike thickness measured by Walker (1987) in the Koolau complex of Oahu is about 50 cm. He gave no estimates of dike lengths, but we can make inferences based on the work of Gartner (1985, 1986) on basaltic dikes of the San Rafael complex, Utah. Gartner (1986, Figures 7 and 8) gives histograms that show a peak frequency at a thickness of about 110 cm and at a length of about 150 m. The median of Gartner's thickness data is also about 100 cm, or roughly twice Walker's value; San Rafael dikes less than 40 cm thick are infrequent compared to the Koolau data, possibly because of poorer exposures of thin dikes. The volume of the median San Rafael dike is about the same as our estimate for the reference fracture based on event counts. Measurements by Walker and by Gartner are similar in that a power law describes the size-frequency data; they are interpreted as fractal sets with an average fractal dimension of about 1.5 in plan view. Despite the difference in median thicknesses, the fractal similarity of log-log plots suggests that the data are

comparable. These are not rigorous comparisons, but they agree with the seismic estimates of fracture volumes. Thus, all estimates of fracture dimensions suggest a maximum fracture length less than 1 km.

Our estimation of V_0 is consistent with statistics of dike measurements and with seismic models of the tremor source, and at first glance it would appear that the bellows model gives a balanced budget: *i.e.*, there are 50,000/22 = 2273 magma injection pulses per year associated with a reference injection pulse of 20 sec, an average volume of 4.4×10^4 m^3 per pulse, and a total magma transport rate of 0.1 km^3 per year. There are, however, kinematic problems with this budget. One problem is the fact that the average of 2273 pulses per year would represent the active magma volume from 5 km down to 60 km depth. In order to satisfy the supply rate, fractures at all depths would have to contribute to near-surface intrusions and eruptions. This is inconsistent with the distribution of long-period events in Figure 3 and with intermittent fracture having length scales less than 1 km. The scale problem is clarified by considering averages over different depth zones.

Summations of data in Figure 1 give 1.60×10^4 min of deep tremor and 0.94×10^4 min for intermediate-depth tremor (the latter includes data from 1 January 1980 through 31 December 1983 not shown in Figure 1). The average gradients of tremor rates are 24.2 min yr^{-1} km^{-1} for 30–60 km depth, 42.7 min yr^{-1} km^{-1} for 5–15 km depth, and 21.0 min yr^{-1} km^{-1} for 5–60 km. If the lower 1/3 of the quiet zone is added to the deep zone and 2/3 to the intermediate zone, then a constant 21 min yr^{-1} km^{-1} satisfies the intervals 5–25 and 25–60 km. Taking 1 km as a hypothetical length scale for stratification of magmatic injection (*i.e.*, compatible with maximum lengths of individual fractures inferred above), the mean gradient (21 min yr^{-1} km^{-1}) corresponds to 63 reference pulses per year per 1-km layer (normalized to a 20 sec injection pulse and averaged over 22 years and 5–60 km).

A reference volume, V_0, that simultaneously fits the stratification, a supply rate of 0.1 km^3/yr, and the areal distribution of hypocenters is nonunique. Let us consider the magmatic budget within a 1-km layer; we can write the following equation:

$$V_0 = k\frac{\phi \Delta S}{n} \quad , \qquad (\mathrm{km}^3) \tag{15}$$

where ΔS is the horizontal cross sectional area of the rock column within which incremental transport is assumed to occur (taken to be a vertical cylinder), ϕ is the yearly ratio defined by the volume of magma in a 1-km layer divided by the volume of that layer, n is the yearly number of injection pulses of volume V_0 associated with measurable tremor in the 1-km layer, and $k = n/n^*$ is the ratio of n to the total number of injection pulses of volume V_0 in the layer required to give the correct yearly magma supply rate. Correlation with supply rate is given by the vertical drift velocity $v = dz/dt$. For the above parameters, the drift velocity is estimated by:

$$v = \frac{0.1}{\Phi \Delta S} \quad , \qquad (\mathrm{km/yr}) \tag{16}$$

where 0.1 is the assumed constant magma supply rate, and Φ is the long term average volume fraction of magma within each layer. In the steady state, ϕ and v are constants, and the former represents the fraction of magma actively transported by the fracture mechanism. When extensional fracture is the only displacement mechanism, $\phi = \Phi$, otherwise ϕ/Φ represents the ratio of fracture transport to other forms of transport and storage.

If all transport events are recorded by tremor, then for constant supply rate V_0 only depends on the area of the path, ΔS, the magma fraction Φ, and the incremental number of events, n. Shaw (1980, p. 248) estimates $\Phi \approx 10^{-5}$ based on compressibility and tensile strength. For $\Phi \approx 10^{-5}$ in Eq. (15) and $V_0 \approx 4.4 \times 10^{-5}$ km^3, and with $n = 63$ pulses per km per year and $k = 1$, ΔS would be much smaller than the total area encompassed in Figure 3 (this area has a radius of about 35 km if one includes Mauna Loa, Kilauea, and Loihi volcanoes). For example, if we reduce ΔS to an area of radius 10 km (314 km^2) and assume that all events are recorded ($k = 1$), we obtain $V_0 \approx 5 \times 10^{-5}$ km^3. But when we use these values ($\Phi = 10^{-5}$, $\Delta S = 314$ km^2) in Eq. (16) we obtain $v \approx 30$ km yr^{-1}. Large values of v can exist transiently, but we assume that the average distance of vertical magma migration per year is much smaller than 30 km. A reasonable fit is obtained by setting $\Delta S = 314$ km^2 (radius = 10 km), $\Phi = 10^{-4}$, and $k = 0.1$, giving $V_0 \approx 5 \times 10^{-5}$ km^3 and $v \approx 3$ km yr^{-1}; this would imply that the

observed events are not only localized but they are a tenth of the number of equivalent volume pulses needed to satisfy the transport. Alternatively, if we set $v \approx 3\ \mathrm{km\,yr^{-1}}$ with $\Phi = 10^{-5}$, $k = 1$, $\Delta S = 3849\ \mathrm{km^2}$ (corresponding to an assumption that tremor events document magma transport throughout the area of radius 35 km depicted in Figure 3), then we obtain $V_0 \approx 6 \times 10^{-4}\ \mathrm{km^3}$, more than an order of magnitude larger than other estimates.

When all three coefficients, k, Φ, and ϕ are allowed to vary, consistent values of drift velocity and fracture volume can be obtained for a variety of assumptions. Also, if there is a threshold of V_0 below which tremor is not detected, then n^* can be arbitrarily large. For example, if the threshold were $V_0 = 10^{-6}\ \mathrm{km^3}$, and $n^* = 10^4$, the transport fraction and drift velocity remain consistent with the above values (if n^* were small, aseismic V_0 would be very large for consistent transport areas, magma fractions, and drift velocities). Large aseismic V_0 would imply that the medium has little strength and magma storage should ensue (sill-like zones), eventually causing seismic instabilities (seemingly a paradox).

With present data we cannot assign unequivocal values to the above parameters. However, their possible ranges are consistent with a relationship between the percolation of fluids through multifractal networks of fractures in solid media and the varieties of acoustic and seismic phenomena that accompany that transport.

A Mean Field Model of Volumetric Relaxation for the Tremor Process

Additional insight into the tremor process can be gained by considering relationships between magma transport, scaling of volume domains, and relaxation times that are simultaneously consistent with a mean trigger force and with the spectrum of tremor periods (dominant seismic period, episode duration, and onset interval). The mean-field properties of transport are associated with packets of fluid, or 'particles,' in a manner analogous to mean field theories of semiconductors. The rock matrix is the analog of a complex lattice within which mass particles are transported in response to force fields acting at appropriate temperatures and crystalline states. The terms 'packet' and 'particle' symbolize configurations of mass (fluid-filled cracks and/or rock matrix) that differ from

the motions of individual atoms, electrons, etc. The mean flow responds to the stress-field *vs.* mass flow-field behavior of the Earth in a manner analogous to voltage *vs.* current behavior of tuned semiconductors. The record of seismic tremor identifies analogous mean-field properties of force *vs.* flow responses of the lithosphere and volcanic edifice.

Despite the fact that the vibrational properties and radiation fields of the tremor mechanism can be described in detail (Chouet, 1988), there are a number of puzzling features of the tremor process that the mean field model should address. For example, what is the cause of a trigger event that activates long-period events and bellows-like motions? The answer is complicated by the fact that each magma injection pulse corresponds to many trigger activations and each tremor episode represents many pulses. This suggests that a tremor episode correlates with a local plexus or dendrite of fluid-filled fractures (Fig. 17*B*) within the hypocentral volume and is consistent with the multifractal character of the tremor history. Accordingly, the trigger mechanism responds to the relaxation frequency of the hypocentral plexus coupled with the characteristic frequencies of the fluid-filled cracks.

By this view, the trigger mechanism punctuates the timing of coupled oscillations of fracture and flow in a manner analogous to the escapement mechanism of a nonlinear clock. Accordingly, it is a self-actuating mechanism. A general relationship between forces, flows, and relaxation times gives some insight into how this may work. The energy comes partly from the stresses of plate tectonic motions and partly from gravitational energy related to buoyancy forces of magma rise. The energetics of the mechanism was analyzed by Chouet (1981). He gave the magnitudes of force couples, pressure drops, and volume increments required to satisfy an average frequency of 1 Hz in the tremor seismogram; we assume this applies to deep tremor of the same frequency. The trigger force applied by the fluid to the crack for increments of opening at 1 per second was estimated to be $F \approx 10^{14}$ dynes.

Assuming that relaxation drives the tremor mechanism, we derive relaxation times consistent with mean-field relationships between the trigger force, F, the mobility of mass transport, μ, and the mass of a transport domain, m_i^*. As in molecular dynamics, mobility represents the drift velocity per unit force: $\mu = v/F$. The relaxation time is given by $\tau^* = m_i^* \mu$ (*e.g.*, Fraser, 1986; asterisks are to avoid confusion with symbols m_i and τ in

the partition equations). The drift velocity, v, is given by Eq. (16). For a supply rate of 0.1 km^3/yr and $\Phi = 10^{-5}$ averaged over the total transport path (cylinder of radius 35 km), we obtain $v = 8 \times 10^{-3}$ cm/sec.

If the trigger mechanism reflects the stress response of a hypocentral domain, then the total mass of that domain contributes to the mobility. A domain of radius 1 km has a mass of the order of 10^{16} gm, giving $\tau_i^* \approx (8 \times 10^{-3})(10^{16})/10^{14} = 0.8$ sec. Although this is not a rigorous forcing frequency, a mean-field theory of multifractal domains seems to be consistent with the scaling of transport parameters. In this respect the theory treats the tremor process in a manner analogous to triggering of electron transport in semiconductors and other solid state devices (Bohr *et al.*, 1984; Gwinn and Westervelt, 1987). Notably, if the trigger frequency were expressed in terms of magma instead of rock mass, then we would have to increase the volume scale and(or) decrease the trigger force in some combination that compensates the mass difference.

When the mean-field analysis is expanded to include the responses of larger-scale geometries, it eventually must include states of stress and relaxation times implied by plate tectonic motions. These are much longer than the time scales of tremor processes in our discussion. But, if the forcing frequency of the trigger mechanism involves relaxation within sets of fluid-filled cracks in the near-field of the hypocenter, then forcing frequencies for activations of different hypocenters involve interactions at distances normally considered to be in the far-field relative to the tremor mechanism. In the fractal context, these near-field and far-field effects are not dynamically separable.

To illustrate, we re-scale the mean-field parameters to describe the larger structures. The drift velocity is the same, and if the magnitude of the force term is not changed, then the scaling refers to analogous correlations of relaxation times and mass domains. Applying these relations to tube-like volumes described in Koyanagi *et al.* (1987) and Ryan (1987), we obtain relaxation times, τ^*, of the orders of magnitude of the average tremor duration (about 25 min). By the same token, the mass of the total subvolcanic cylinder of radius 35 km and length 60 km correlates with the order of magnitude of the average onset interval between tremor episodes (about 16 days). We do not argue that the scaling is correct, but a spectrum of relaxation times that simultaneously describes

forcing frequencies of tremor spectra, duration spectra, and spectra of onset times must be hierarchical over many volume domains that are clustered in the fractal sense. The 'plumbing system,' 'columnar distribution,' and 'compartmental' sources for eruptive loci in Hawaii, identified by the summit locations of Kilauea, Mauna Loa, and Loihi volcanoes (Koyanagi *et al.*, 1987, pp. 1248–1257), are qualitative terms for the fractal geometry of these dynamical processes.

There are testable distinctions between a mean field model and a conduit model (*e.g.*, Eaton and Murata, 1960) or a model that implies a neck or throttle in a plexus of conduits and dike injections (*e.g.*, Ryan, 1987, in press). This is because fracture is the rate-limiting control on transport in our model; we minimize the role of continuous flow except within the upper 5 km where stress states permit conduits to remain open independently of magma pressure fluctuations. During magma ascent from the asthenosphere (Fig. 17), solid state stress relaxation is sufficiently rapid and interactive with magma pressures that fractures open and close transiently over relatively small length scales. The model by Ryan (1987, in press) invokes dike injections, but he emphasizes continuity between a neutral-buoyancy horizon at a depth of about 3 km and a cylindrical 'primary conduit' extending to a depth of about 40 km below Kilauea. High transport rates in this vertical cylinder correspond to special sets of parameters in Eqs. (15) and (16) that give large localized magma fractions and(or) drift velocities v.

When the term 'conduit' is applied to sets of densely clustered magma injections (Ryan, in press) it is consistent with the concept of variable clustering in a fractal percolation model such as we describe. In that sense, Ryan's model can be viewed as an end member of the clustering model. However, we do not consider the 'quiet zone' at 15-30 km in our model to be a unique neck or throttle in the flow field. It may represent a region of more frequent magma injections that produce vibrations below detection threshold. If so, it could more closely approximate the CGMN condition. A similar situation may apply to the region between the asthenosphere and the zone of deep tremor in Figure 3.

DISCUSSION AND CONCLUSIONS

If the tremor process is interpreted to represent nonlinear resonances, then local portions of the system apparently can be tuned to a specific regime, such as the mode-locking regime (perhaps to a single attractor within a regime), while other portions are more globally tuned to the CGMN and(or) chaotic regimes. This is not a contradiction in a rheologically diversified medium. Local spectra of long-period events and tremor reflect the geometries of magma concentrations in fluid-filled cracks, while the spectra of tremor durations and onset times reflect the geometries of sets of hypocentral domains and their clustering within the lithosphere. The scaling of transport parameters in Eqs. (15) and (16) and structures described by Koyanagi *et al.* (1987) and Ryan (1987) support this interpretation. Such a system of attractors is largely self-regulating.

Many uncertainties and paradoxes persist in our understanding of the tremor process. Some aspects relate to the fact that relationships between attractor domains in the mode-locked, CGMN, and chaotic domains may be unpredictable, even though they are aspects of the same system of coupled oscillators, because of sensitive dependence on initial conditions. This situation is unsatisfactory to the extent that we are unable to correlate these regimes with volcanic behavior. We conclude by indicating data needed to elucidate the relationships between fractal geometry and dynamics. These data should address contradictions in the observations, such as the following:

(1) The geometry of time series of tremor intermittencies is roughly self-similar, as expressed by singularity spectra of episode durations and onset intervals of deep and intermediate-depth tremor, but the respective time series differ greatly in detail (see Figures 1 and 4).

(2) The total durations of tremor over the intermediate and deep zones divided by depth intervals and length of the record give similar values of average rates per unit depth. If these values represent moment rates per unit depth, and if moment rates correlate with magma transport rates per unit depth, then the gradients fluctuate in time and are not in phase with each other or with the total supply rate inferred from summit tilt data; compare depth zones in Figures 1 and 4 with supply rates in Dzurisin *et al.* (1984).

(3) Rate fluctuations with depth are sometimes correlated, according to Koyanagi *et al.* (1987, p. 1256), who state: "After sustained high rates of shallow intrusions, deep long-period events tend to persist and the rate of reduced displacement of deep harmonic tremor tends to increase." A similar point was made by J. P. Eaton (written communication, 24 June 1987) regarding observations prior to 1961. These may be failure cascades (Shaw, 1980), suggesting that coupling of shallow and deeper tremor cannot be ignored.

(4) Because the 'quiet zone' lies between the deep and intermediate zones, fluctuations in gradients with time imply variable rates of magma accumulation in this zone if the tremor responses are not in phase (see discussion of Eqs. (15) and (16)).

(5) If different depth zones are not mutually in phase and are not in phase with fluctuations in the total magma supply rate, then transient storage exists at all depths and(or) transient fluctuations exist in lateral transport rates at all depths.

(6) Discrepancies between cumulative reduced displacements for tremor events and the total magma supply rate (Aki and Koyanagi, 1981) imply either that: (a) moment rates inferred from source models of tremor are correct, but the catalog of events is incomplete, or (b) deep magma transport correlates with source mechanisms that include aseismic behavior and(or) moments of short-period earthquakes (*e.g.*, relaxation effects of short-period events represented by viscous losses within a plexus of fluid-filled fractures; *cf.*, seismic efficiencies in Shaw, 1980, Fig. 18).

(7) The ratios of domain mass, m_i^*, to trigger force, F, in a mean-field description of tremor time scales are large. Because the mean-field model refers to steady-state balances, we infer that there are effects of very long-range coordination in the tremor process, and(or) the force is excessive and the triggering mechanism requires reevaluation.

This list does not exhaust questions raised by the singularity analysis, but it identifies some important deficiencies of documentation. These points might be boiled down to a central paradox in which two statements seem equally true: (a) We can account for the budget of magma transport by counting the observed tremor episodes and fracture dimensions multiplied by a constant proportion (k in Eq. (15)) of unrecorded events; *i.e.*, the magma supply budget is basically measured by tremor durations. (b) Transport rates are decoupled from tremor rates in a way that minimizes seismic activity and maximizes

magma storage and(or) aseismic transport in some regions; *i.e.*, the major portion of magma transport is not measured by tremor durations.

A glaring problem is the lack of information concerning the relationship between tremor amplitudes and episode durations at the limit of seismic detection. This is important to the evaluation of $\alpha_{\min}$ in the singularity spectra of Figure 14, to the limiting fractal dimensions in Figure 7, to issues of phase correlations between depth zones, and therefore to issues of correlations between tremor moment and magma storage as a function of depth. Storage events are implied over all depths if tremor episodes of decreasing amplitudes increase in numbers without limit. In that case, the limiting slopes in Figure 7 that appear to define a fractal dimension $D = 0$, and the low values of $\alpha_{\min}$ in Figure 14, are artifacts of roll-off in the documentation of episodes and amplitudes. Alternatively, if the truncation in the counts of tremor events are real, then there is a physical limit below which tremor cannot be activated, and there are fracture dimensions below which significant increments of magma transport do not occur (*i.e.*, the roll-off is physical, and relatively large-scale fracture rather than small-scale fracture and(or) porous-media flow is the rate-limiting mechanism of transport).

These alternatives may require new interpretations of earthquake source mechanisms. Existing energetic analyses of the trigger mechanism for long-period events may be incomplete, implying that we do not fully understand the relationship between fracture propagation and fluid transport. By any interpretation, the missing information concerns the role of magmatic interactions with the earthquake mechanism at all time scales. Apparently we cannot treat long-period and short-period earthquakes as phenomena with distinctly different and separable source mechanisms. In order to clarify these relationships, we need data of the following kinds: (1) catalogs that include composite indexing in space and time of both long- and short-period events, (2) assessment of event frequencies below $M = 1$, (3) more complete documentation of earthquake spectra at frequencies below 1 Hz, (4) improved resolution of amplitude data for tremor episodes, (5) more complete analysis of the geometries of radiation fields of different types of events, and (6) improved rheological insight into the nature of the fracture process in materials that involve a fluid phase that has significant (and over short time scales, potentially very high) vapor pressures.

Some relevant studies are currently in progress. With even some of this information in hand, and the knowledge that theories of coupled nonlinear oscillators are appropriate, we may be able to confirm the nature of volcanic attractors. It is possible that some of the contradictions we have noted are dynamical artifacts of multifractal singularity distributions. It is therefore imperative to decrease uncertainties caused by limited sample size, perhaps by extending the method to include short-period earthquakes. The application of singularity analysis to the earthquake process has much in common with applications to theories of turbulence in fluids, oscillations of magnetic fields in conducting fluids (*e.g.*, the core dynamo) and ordering in solid state electronic devices. Advances in these areas of study may permit us to map out the characteristic dynamical regimes and universalities that are most relevant to the coupling of tectonic and volcanic evolutions and to the evaluation of earthquake and eruption hazards in Hawaii.

ACKNOWLEDGMENTS

We owe special thanks to Bob Koyanagi of the Hawaiian Volcano Observatory for data and for discussions of the tremor process. The manuscript was read by Jerry Eaton and Bob Decker, both of whom added greatly to a clearer appreciation of Hawaiian volcanism.

REFERENCES

Aki, K. and R. Koyanagi, Deep volcanic tremor and magma ascent mechanism under Kilauea, Hawaii, *J. Geophys. Res., 86,* pp. 7095–7109, 1981.

Bak, P., The Devil's staircase, *Phys. Today, 39,* pp. 38–45, 1986.

Bergé, P., Y. Pomeau, and C. Vidal, *Order Within Chaos,* N.Y., John Wiley and Sons, 1984.

Bohr, T., P. Bak, and M.H. Jensen, Transition to chaos by interaction of resonances in dissipative systems. II. Josephson junctions, charge-density waves, and standard maps, *Phys. Rev. A., 30,* pp. 1970–1981, 1984.

Brandstätter, A., J. Swift, H.L. Swinney, A. Wolf, J.D. Farmer, E. Jen, and P.J. Crutchfield, Low-dimensional chaos in a hydrodynamic system, *Phys. Rev. Lett., 51,* pp. 1442–1445, 1983.

Chouet, B., Ground motion in the near field of a fluid-driven crack and its interpretation in the study of shallow volcanic tremor, *J. Geophys. Res., 86,* pp. 5985–6016, 1981.

Chouet, B., Dynamics of a fluid-driven crack in three dimensions by the finite difference method, *J. Geophys. Res., 91,* pp. 13,967–13,992, 1986.

Chouet, B., Resonance of a fluid-driven crack: radiation properties and implications for the source of long-period events and harmonic tremor, *J. Geophys. Res., 93,* 1988.

Chouet, B., R.Y. Koyanagi, and K. Aki, Origin of volcanic tremor in Hawaii. Part II. Theory and discussion, in *Volcanism in Hawaii,* edited by R.W. Decker, T.L. Wright, and P.H. Stauffer, pp. 1259–1280, *U.S. Geol. Surv. Prof. Pap. 1350,* 1987.

Clague, D.A. and G.B. Dalrymple, The Hawaiian–Emperor volcanic chain. Part I. Geologic evolution, in *Volcanism in Hawaii,* edited by R.W. Decker, T.L. Wright, and P.H. Stauffer, pp. 5–54, *U.S. Geol. Surv. Prof. Pap. 1350,* 1987.

Crutchfield, J.P., J.D. Farmer, N.H. Packard, and R.S. Shaw, Chaos, *Sci. Am., 255 (No.6),* pp. 46–57, 1986.

Decker, R.W., Dynamics of Hawaiian volcanoes: an overview, in *Volcanism in Hawaii,* edited by R.W. Decker, T.L. Wright, and P.H. Stauffer, pp. 997–1018, *U.S. Geol. Surv. Prof. Pap. 1350,* 1987.

Dzurisin, D., R.Y. Koyanagi, and T.T. English, Magma supply and storage at Kilauea Volcano, Hawaii, 1956–1983, *J. Volc. Geoth. Res., 21,* pp. 177–206, 1984.

Eaton, J.P., and K.J. Murata, How volcanoes grow, *Science, 132,* pp. 925–938, 1960.

Essex, C., T. Lookman, and M.A.H. Nerenberg, The climate attractor over short time scales, *Nature, 326,* pp. 64–66, 1987.

Feigenbaum, M.J., Quantitative universality for a class of nonlinear transformations, *J. Stat. Phys., 19,* pp. 25–52, 1978.

Feigenbaum, M.J., The onset spectrum of turbulence, *Phys. Lett., 74A,* pp. 375–378, 1979.

Feigenbaum, M.J., Universal behavior in nonlinear systems, *Los Alamos Science, 1,* pp. 4–27, 1980.

Fein, A.P., M.S. Heutmaker, and J.P. Gollub, Scaling at the transition from quasiperiodicity to chaos in a hydrodynamic system, *Physica Scripta, T9,* pp. 79–84, 1985.

Fraser, D.A., *The Physics of Semiconductor Devices,* Oxford, Clarendon Press, 1986.

Fraser, A.M. and M.L. Swinney, Independent coordinates for strange attractors from mutual information, *Phys. Rev. A., 33,* pp. 1134–1140, 1986.

Gartner, A.E., *Geometry and emplacement history of a basaltic intrusive complex, San Rafael Swell and Capitol Reef Areas, Utah,* M.Sc. Dissertation, Dept. Geol., San Jose State University, 1985.

Gartner, A.E., Geometry, emplacement history, petrography, and chemistry of a basaltic intrusive complex, San Rafael and Capitol Reef areas, Utah, *U.S. Geological Survey, Open-File Report 86-81,* 1986.

Gollub, J.P. and S.V. Benson, Many routes to turbulent convection, *J. Fluid Mech., 100,* pp. 449–470, 1980.

Grassberger, P., Do climatic attractors exist?, *Nature, 323*, pp. 609–612, 1986.

Grassberger, P. and I. Procaccia, Characterization of strange attractors, *Phys. Rev. Lett., 50*, pp. 346–349, 1983.

Guevara, M.R., L. Glass, and A. Shrier, Phase locking, period-doubling bifurcations, and irregular dynamics in periodically stimulated cardiac cells, *Science, 214*, pp. 1350–1353, 1981.

Gwinn, E.G., and R.M. Westervelt, Scaling structure of attractors at the transition from quasiperiodicity to chaos in electronic transport in Ge, *Phys. Rev. Lett., 59*, pp. 157–160, 1987.

Halsey, T.C., M.H. Jensen, L.P. Kadanoff, I. Procaccia, and B.I. Shraiman, Fractal measures and their singularities: the characterization of strange sets, *Phys. Rev. A., 33*, pp. 1141–1151, 1986.

Hentschel, H.G.E., and I. Procaccia, The infinite number of generalized dimensions of fractals and strange attractors, *Physica 8D*, pp. 435–444, 1983.

Hill, D.P., A model for earthquake swarms, *J. Geophys. Res., 82*, pp. 1347–1352, 1977.

Hirsch, J.E., B.A. Huberman, and D.J. Scalapino, Theory of intermittency, *Phys. Rev. A, 25*, pp. 519–532, 1982.

Holcomb, R.T., Eruptive history and long-term behavior of Kilauea volcano, in *Volcanism in Hawaii*, edited by R.W. Decker, T.L. Wright. and P.H. Stauffer, pp. 261–350, *U.S. Geol. Surv. Prof. Pap. 1950*, 1987.

Jackson, E.D. and H.R. Shaw, Stress fields in central portions of the Pacific plate: delineated in time by linear volcanic chains, *J. Geophys. Res., 80*, pp. 1861–1874, 1975.

Jackson, E.D., E.A. Silver, and G.B. Dalrymple, Hawaiian–Emperor chain and its relation to Cenozoic circumpacific tectonics, *Geol. Soc. Am. Bull., 83*, pp. 601–618, 1972.

Jackson, E.D., H.R. Shaw, and K.E. Bargar, Calculated geochronology and stress field orientations along the Hawaiian chain, *Earth Planet. Sci. Letts., 26,* pp. 145–155, 1975.

Jeffries, C.D., Chaotic dynamics of instabilities in solids, *Physica Scripta, T9,* pp. 11–26, 1985.

Jensen, M.H., P. Bak, and T. Bohr, Transition to chaos by interaction of resonances in dissipative systems. I. Circle maps, *Phys. Rev. A, 30,* pp. 1960–1969, 1984.

Jensen, M.H., L.P. Kadanoff, A. Libschaber, I. Procaccia, and J. Stavans, Global universality at the onset of chaos: results of a forced Rayleigh–Bénard experiment, *Phys. Rev. Lett., 55,* pp. 2798–2801, 1985.

Jensen, R.V., Classical chaos, *Am. Scientist, 75,* pp. 168–181, 1987.

Karpin, T.L. and C.H. Thurber, The relationship between earthquake swarms and magma transport: Kilauea volcano, Hawaii, *Pure Appl. Geophys., 125,* pp. 971–991, 1987.

Klein, F.W., Patterns of historical eruptions at Hawaiian volcanoes, *J. Volc. Geoth. Res., 12,* pp. 1–35, 1982.

Klein, F.W., R.Y. Koyanagi, J.S. Nakata, and W.R. Tanigawa, The seismicity of Kilauea's magma system, in *Volcanism in Hawaii,* edited by R.W. Decker, T.L. Wright, and P.H. Stauffer, pp. 1019–1185, *U.S. Geol. Surv. Prof. Pap. 1350,* 1987.

Koyanagi, R.Y., B. Chouet, and K. Aki, Origin of volcanic tremor in Hawaii. Part I. Data from the Hawaiian Volcano Observatory, in *Volcanism in Hawaii,* edited by R.W. Decker, T.L. Wright, and P.H. Stauffer, pp. 1221–1257, *U.S. Geol. Surv. Prof. Pap. 1350,* 1987.

Lichtenberg, A.J. and M.A. Lieberman, *Regular and Stochastic Motion,* N.Y., Springer-Verlag, 1983.

Lorenz, E.N., Deterministic nonperiodic flow, *J. Atmospheric Sciences, 20,* pp. 130–141, 1963.

Lorenz, E.N., The problem of deducing the climate from the governing equations, *Tellus, 16,* pp. 1–11, 1964.

Lorenz, E.N., On the prevalence of aperiodicity in simple systems, *Lecture Notes in Math., 755,* pp. 53–77, 1979.

Mandelbrot, B.B., Intermittent turbulence in self-similar cascades: divergence of high moments and dimension of the carrier, *J. Fluid Mech., 62,* pp. 331–358, 1974.

Mandelbrot, B.B., *The Fractal Geometry of Nature,* W.H. Freeman, San Francisco, 1982.

Mandelbrot, B.B., Fractal measures (their infinite moment sequences and dimensions) and multiplicative chaos: early works and open problems, in G. Mayer-Kress, *Dimensions and Entropies in Chaotic Systems,* pp. 19–27, N.Y., Springer–Verlag, 1986.

Manneville, P., Intermittency, self-similarity and 1/f spectrum in dissipative dynamical systems, *J. Phys. (Paris), 41,* pp. 1235–1243, 1980.

Manneville, P. and Y. Pomeau, Intermittency and the Lorenz model, *Phys. Lett., 75A,* pp. 1–2, 1979.

May, R.M., Simple mathematical models with very complicated dynamics, *Nature, 261,* pp. 459–467, 1976.

Mayer-Kress, G. and S.P. Layne, Dimensionality of the human electro-encephalogram, *N.Y. Acad. Sci., Annals, 504,* pp. 62–87, 1987.

Moon, F.C., *Chaotic vibrations,* N.Y., John Wiley and Sons, 1987.

Moore, J.G., Subsidence of the Hawaiian Ridge, in *Volcanism in Hawaii,* edited by R.W. Decker, T.L. Wright, and P.M. Stauffer, pp. 85–100, *U.S. Geol. Surv. Prof. Pap. 1350,* 1987.

Moore, J.G. and J.F. Campbell, Age of tilted reefs, Hawaii, *J. Geophys. Res., 92,* pp. 2641–2646, 1987.

Nicolis, C. and G. Nicolis, Is there a climate attractor?, *Nature, 311,* pp. 529–532, 1984.

Packard, N.H., J.P. Crutchfield, J.D. Farmer, and R.S. Shaw, Geometry from time series, *Phys. Rev. Lett., 45,* pp. 712–716, 1980.

Pollard, D.D., Derivation and evaluation of a mechanical model for sheet intrusions, *Tectonophys., 19,* pp. 233–269, 1973.

Pollard, D.D., On the form and stability of open hydraulic fractures in the Earth's crust, *Geophys. Res. Letts., 3,* pp. 513–516, 1976.

Pomeau, Y. and P. Manneville, Intermittent transition to turbulence in dissipative dynamical systems, *Commun. Math. Phys., 74,* pp. 189–197, 1980.

Procaccia, I. and H. Schuster, Functional renormalization-group theory of universal 1/f noise in dynamical systems, *Phys. Rev. A., 28,* pp. 1210–1212, 1983.

Procaccia, I., The characterization of fractal measures as interwoven sets of singularities: global universality at the transition to chaos, in *Dimensions and Entropies in Chaotic Systems,* edited by G. Mayer-Kress, pp. 8–18, Springer–Verlag, N.Y., 1986.

Ryan, M.P., Elasticity and contractancy of Hawaiian olivine tholeiite and its role in the stability and structural evolution of subcaldera magma reservoirs and rift systems, in *Volcanism in Hawaii,* edited by R.W. Decker, T.L. Wright, and P.H. Stauffer, pp. 1395–1447, *U.S. Geol. Surv. Prof. Pap. 1350,* 1987.

Ryan, M.P., The mechanics and three-dimensional internal structure of active magmatic systems: Kilauea volcano, Hawaii, *J. Geophys. Res.*, in press.

Schuster, H.G., *Deterministic Chaos*, 2nd. Ed., N.Y., VCH Publishers, 1988.

Shaw, H.R., Mantle convection and volcanic periodicity in the Pacific: evidence from Hawaii, *Bull. Geol. Soc. Am., 84,* pp. 1505–1526, 1973.

Shaw, H.R., The fracture mechanisms of magma transport from the mantle to the surface, in *Physics of Magmatic Processes,* edited by R.B. Hargraves, pp. 201–264, Princeton Univ. Press, Princeton, N.J., 1980.

Shaw, H.R., Uniqueness of volcanic systems, in *Volcanism in Hawaii,* edited by R.W. Decker, T.L. Wright, and P.H. Stauffer, pp. 1357–1394, *U.S. Geol. Surv. Prof. Pap., 1350,* 1987a.

Shaw, H.R., The periodic structure of the natural record, and nonlinear dynamics, *Eos, Trans. Am. Geophys. Union, 68,* pp. 1651–1665, 1987b.

Shaw, H.R., Mathematical attractor theory and plutonic-volcanic episodicity, *Earth Evolution Sciences, in press.*

Shaw, H.R. and D.A. Swanson, Eruption and flow rates of flood basalts, in *Columbia River Basalt Symposium, 2nd, Proceedings,* edited by E.H. Gilmour and D. Stradling, pp. 271–299, Eastern Washington State College Press, Cheney, WA, 1970.

Shaw, H.R. and B. Chouet, Kilauean volcanic tremor as a case study of multifractal attractor dynamics, *Abstracts, Symposium on How Volcanoes Work,* p. 232, Hilo, HI, January 19–25, 1987.

Shaw, H.R., E.D. Jackson, and K.E. Bargar, Volcanic periodicity along the Hawaiian–Emperor chain, *Am. J. Sci., 280-A,* pp. 667–708, 1980.

Shaw, Robert, Strange attractors, chaotic behavior, and information flow, *Z. Naturforsch., 36a,* pp. 80–112, 1981.

Shaw, Robert, *The Dripping Faucet as a Model Chaotic System,* Aerial Press, Santa Cruz, CA, 1984.

Shenker, S.J., Scaling behavior in a map of a circle onto itself: empirical results, *Physica, 5D,* pp. 405–411, 1982.

Testa, J., J. Perez, and C. Jeffries, Evidence for bifurcation and universal chaotic behavior in nonlinear semiconducting devices, Lawrence Berkeley Laboratory, University of California, *LBL-13719,* pp. 1–33, 1982.

Thompson, J.M.T., and H.B. Stewart, *Nonlinear Dynamics and Chaos,* N.Y., John Wiley and Sons, 1986.

Vallis, G.K., El Niño: a chaotic dynamical system?, *Science, 232*, pp. 243–245, 1986.

Walker, G.P.L., The dike complex of Koolau Volcano, Oahu: internal structure of a Hawaiian rift zone, in *Volcanism in Hawaii*, edited by R.W. Decker, T.L. Wright, and P.H. Stauffer, pp. 961–993, *U.S. Geol. Surv. Prof. Pap. 1350*, 1987.

FIGURE CAPTIONS

Figure 1. Record of tremor durations for individual events used in this study: A. Deep events (30–60 km) from 1 January 1962 through 31 December 1983: total, 1.60×10^4 min; average, 727 min yr^{-1}. B. Intermediate-depth events (5–15 km) from 1 January 1962 through 31 December 1979. Durations exceeding 99 min occurred on 10/25/65 (210 min), 9/6/69 (480 min), and 10/11/71 (195 min); data after 31 December 1979 available as daily sums: total, 7990 min to 1980; daily readings add 1410 min through 1983. 22-year total, 0.94×10^4 min; average, 427 min yr^{-1}.

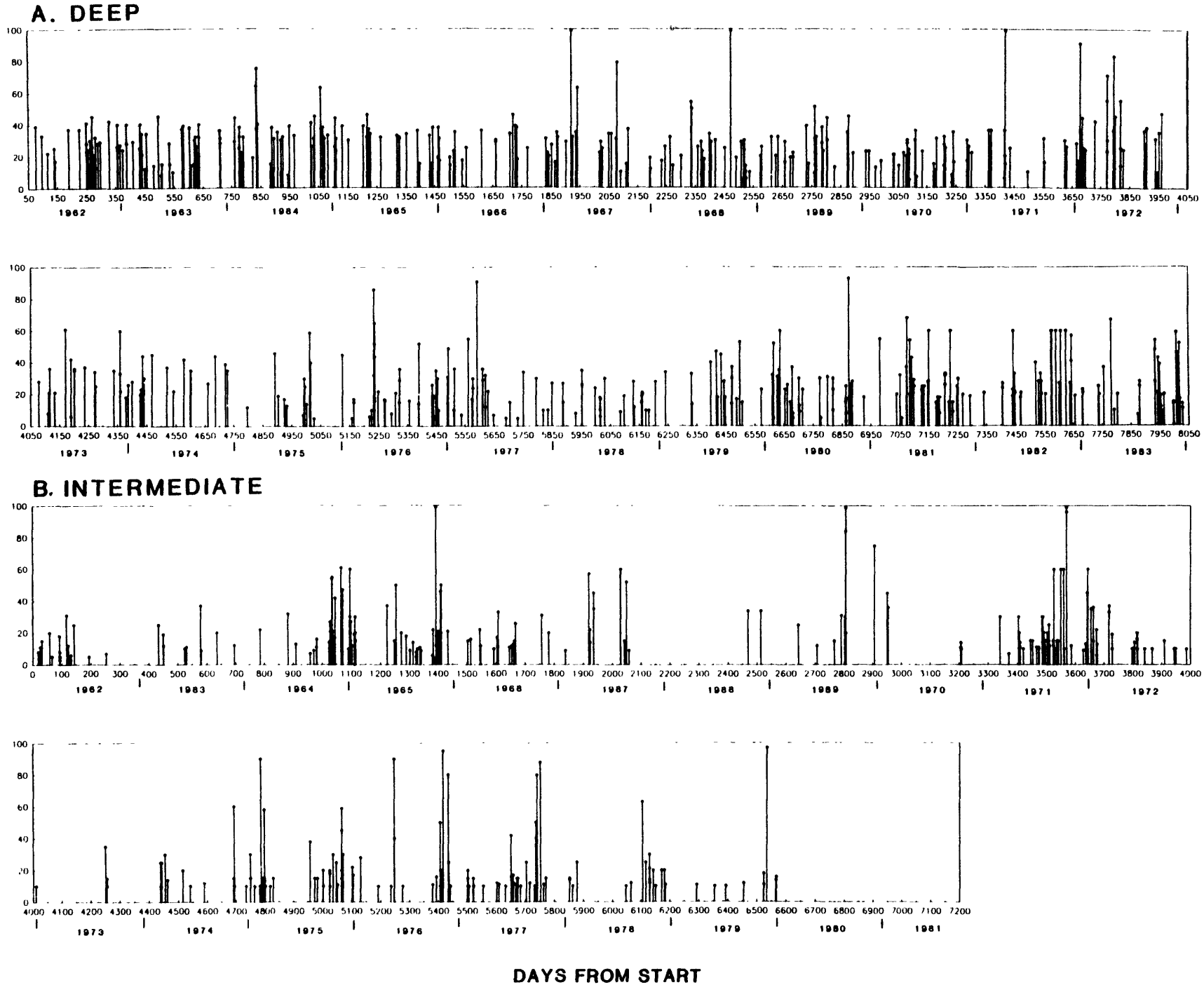
A. DEEP
B. INTERMEDIATE
EVENT DURATION (MINUTES)
DAYS FROM START
1962
1963
1964
1965
1966
1967
1968
1969
1970
1971
1972
1973
1974
1975
1976
1977
1978
1979
1980
1981
1982
1983

Fig. 1.

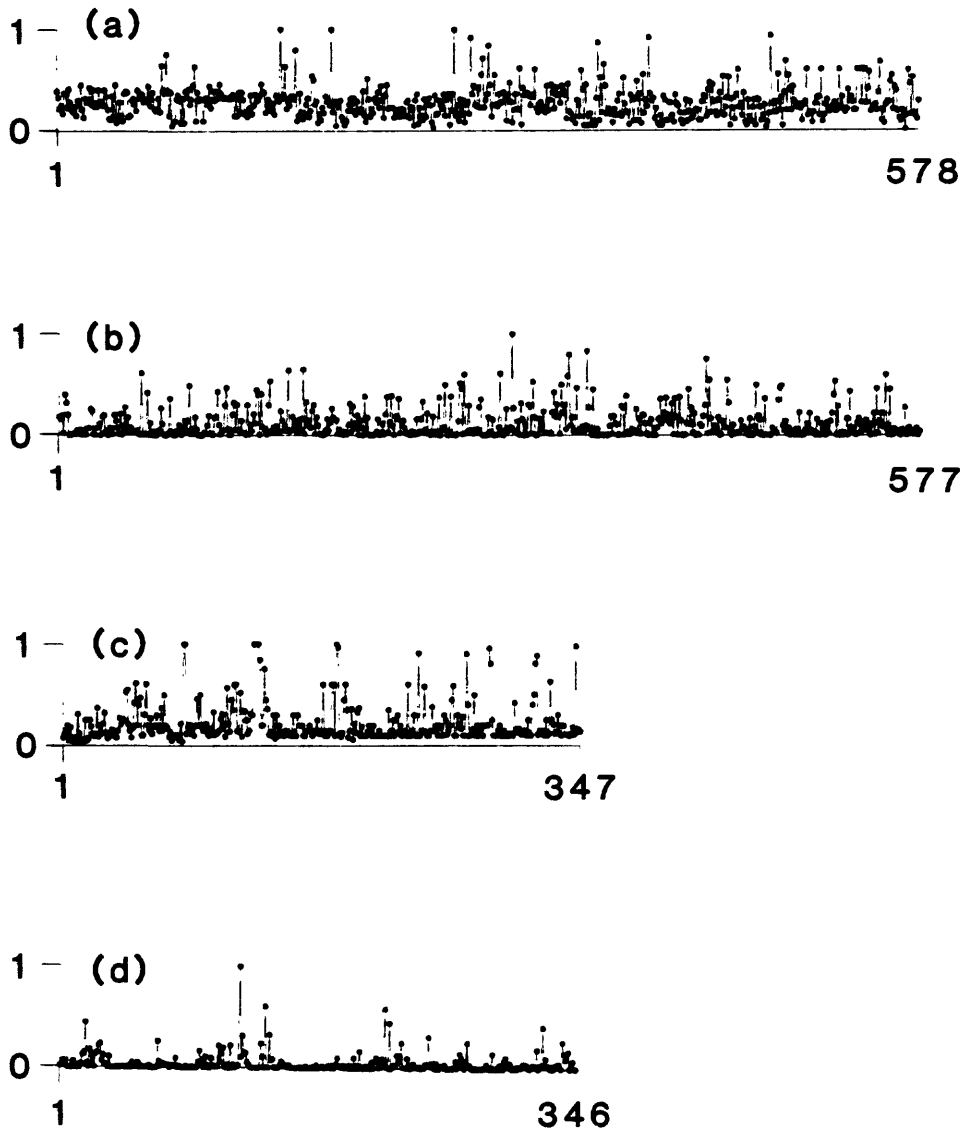

Figure 2. Durations and onset intervals in Figure 1 normalized to unit range: (a) Deep durations normalized to 99 min. (b) Deep intervals (days between onset of tremor episodes) normalized to greatest value (117.92 days). (c) Intermediate-depth durations normalized to 99 min. (d) Intermediate-depth intervals normalized to greatest value (412.00 days).

Figure 3. Schematic illustration of short-period and long-period earthquake hypocenters beneath Kilauea (redrawn from Klein *et al.* , 1987 (Figs. 43.16 and 43.17), and Koyanagi *et al.* , 1987 (Fig. 45.27)). Dots are short-period earthquakes of magnitudes greater than 2 to 1980 and greater than 1 after 1980 (cross-hatching indicates greatest density of events). Heavy dashed lines and triangles are regions of long-period events of magnitudes greater than about 1 (intermediate depth) to 1.5 (deep) during roughly same time period; horizontal lines demark intermediate-depth (5–15 km) and deep (30–60 km) tremor episodes. Interval 15–30 km depth is 'quiet zone' of least seismic activity at detectable magnitudes: A. Hypocenters within a vertical swath trending west-northwest to east-southeast. B. Hypocenters within a vertical swath trending southwest to northeast. C. Epicentral plot of southeast portion of island that includes Kilauea, Mauna Loa, and part of Loihi volcanoes, showing swaths of hypocenters in A and B.

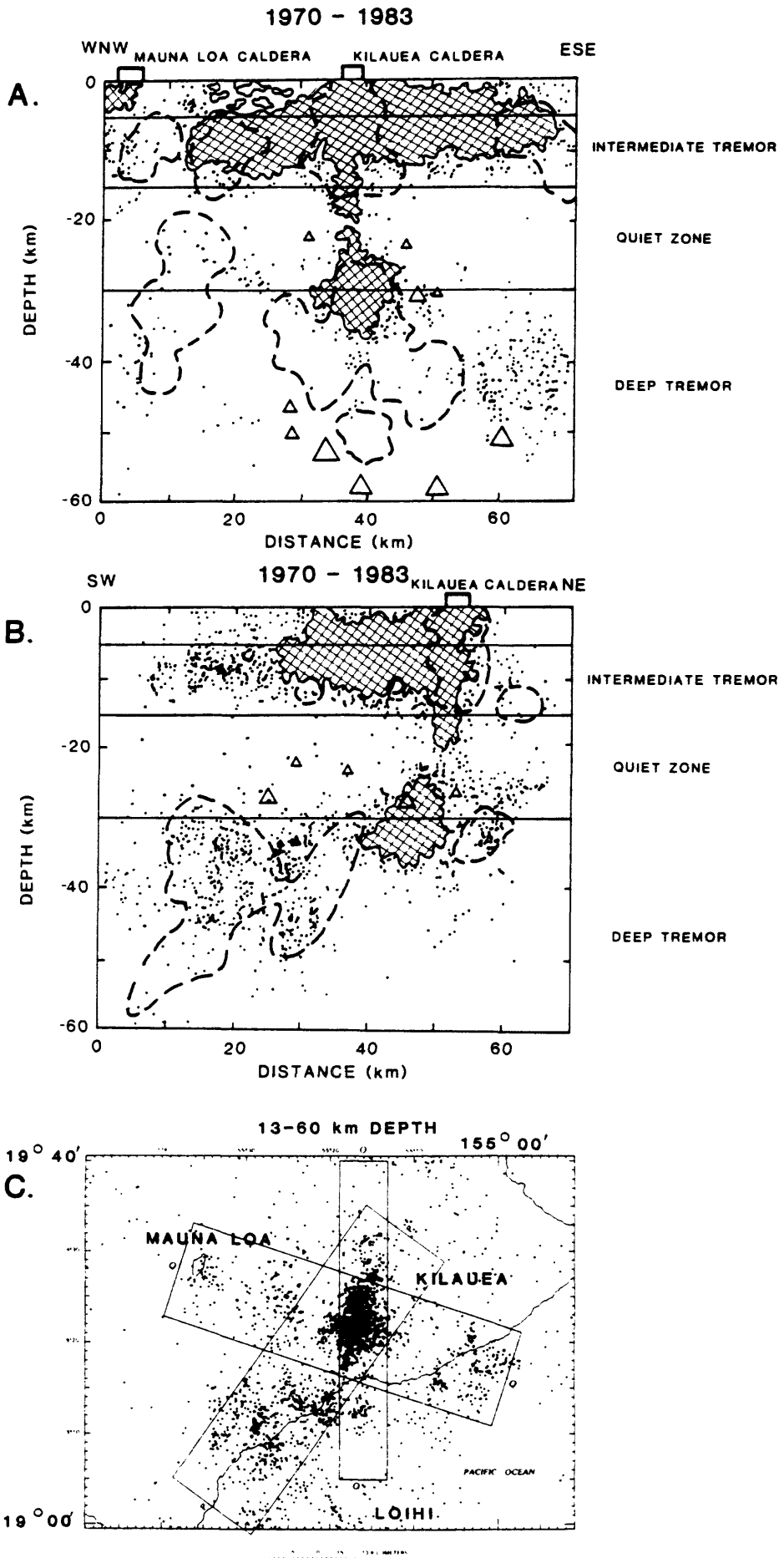
1970 - 1983
WNW
MAUNA LOA CALDERA
KILAUEA CALDERA
ESE
A.
0
-20
-40
-60
DEPTH (km)
INTERMEDIATE TREMOR
QUIET ZONE
DEEP TREMOR
0
20
40
60
DISTANCE (km)
SW
1970 - 1983
KILAUEA CALDERA
NE
B.
0
-20
-40
-60
DEPTH (km)
INTERMEDIATE TREMOR
QUIET ZONE
DEEP TREMOR
0
20
40
60
DISTANCE (km)
13-60 km DEPTH
19° 40'
155° 00'
C.
MAUNA LOA
KILAUEA
PACIFIC OCEAN
LOIHI
19° 00'

Fig. 3

Figure 4. Logarithms of tremor rates *vs.* time calculated from Figure 1; rate (min day^{-1}) defined as episode duration divided by difference of onset times between episodes: A. Deep tremor. B. Intermediate-depth tremor.

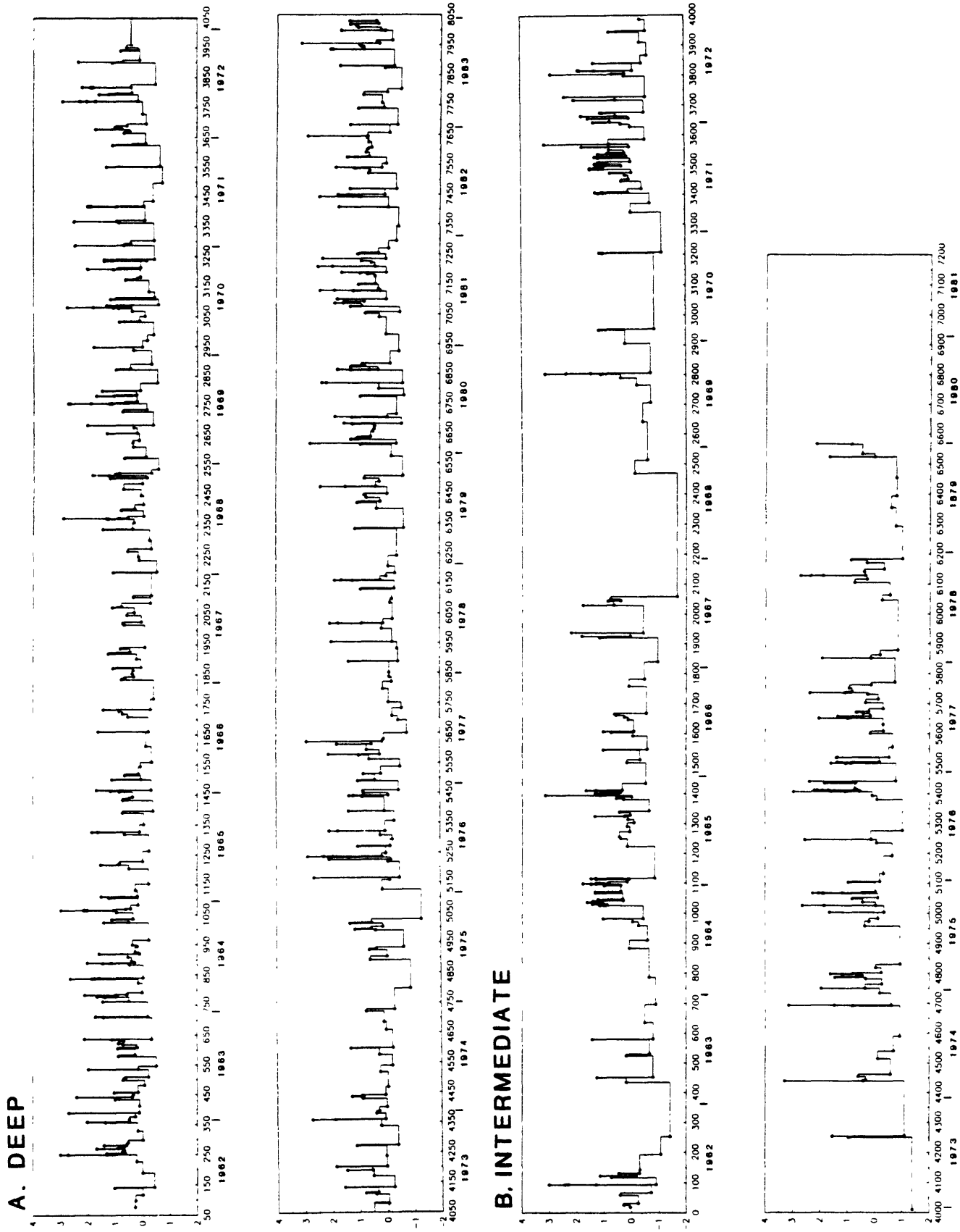
A. DEEP
B. INTERMEDIATE
LOG10 RATE (MINUTES PER DAY)
DAYS FROM START

Fig. 4.

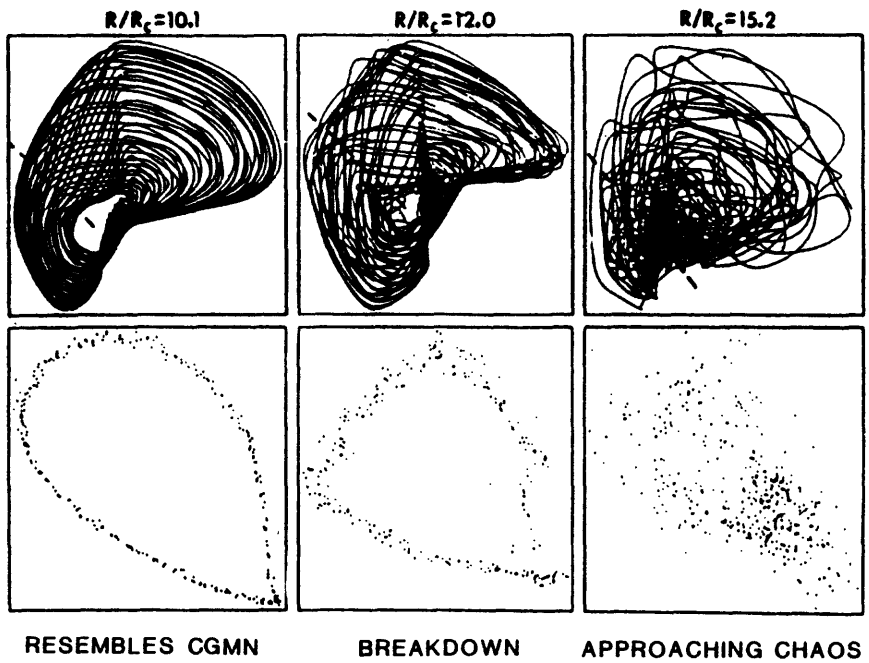

Figure 5. Phase portraits (top) and Poincaré sections (bottom) for forced convection (Couette–Taylor flow) near onset of turbulence (chaotic regime) (from Brandstätter *et al.* , 1983). Top gives 2-dimensional plots of radial velocity vectors from Doppler velocimetry at given time, t, and time shifted by $t + 130$ (ms), as function of Reynolds number, R (R_c is critical value for formation of Taylor vortices). Bottom shows sections of 3-dimensional phase space in which third dimension is velocity vector at $t + 260$ (ms); sections located by dashed lines. Poincaré sections resemble sine circle map at onset of chaos and phase plots of oscillatory Rayleigh–Bénard convection excited in second mode (Jensen *et al.*, 1985).

Figure 6. Phase portraits (return maps) of deep tremor based on data of Figure 1 (subdivided into six parts of about same numbers of recurrences, and total for 22 years): dots give one reading *vs.* next reading plotted in sequence of Figure 2; solid lines connect sequences of readings, as in return maps of quadratic equations (*e.g.*, Feigenbaum, 1980) and sine circle map (*e.g.*, Jensen *et al.*, 1984, Fig. 1). Clustering of points on the plane x_{n+1} *vs.* x_n is analogous to clusters on the circle map, *i.e.*, circle map is analog of Poincaré section of portrait of coupled oscillator (see Fig. 5; Fig. 16*D*, panel b): A. Durations (min).

DURATIONS

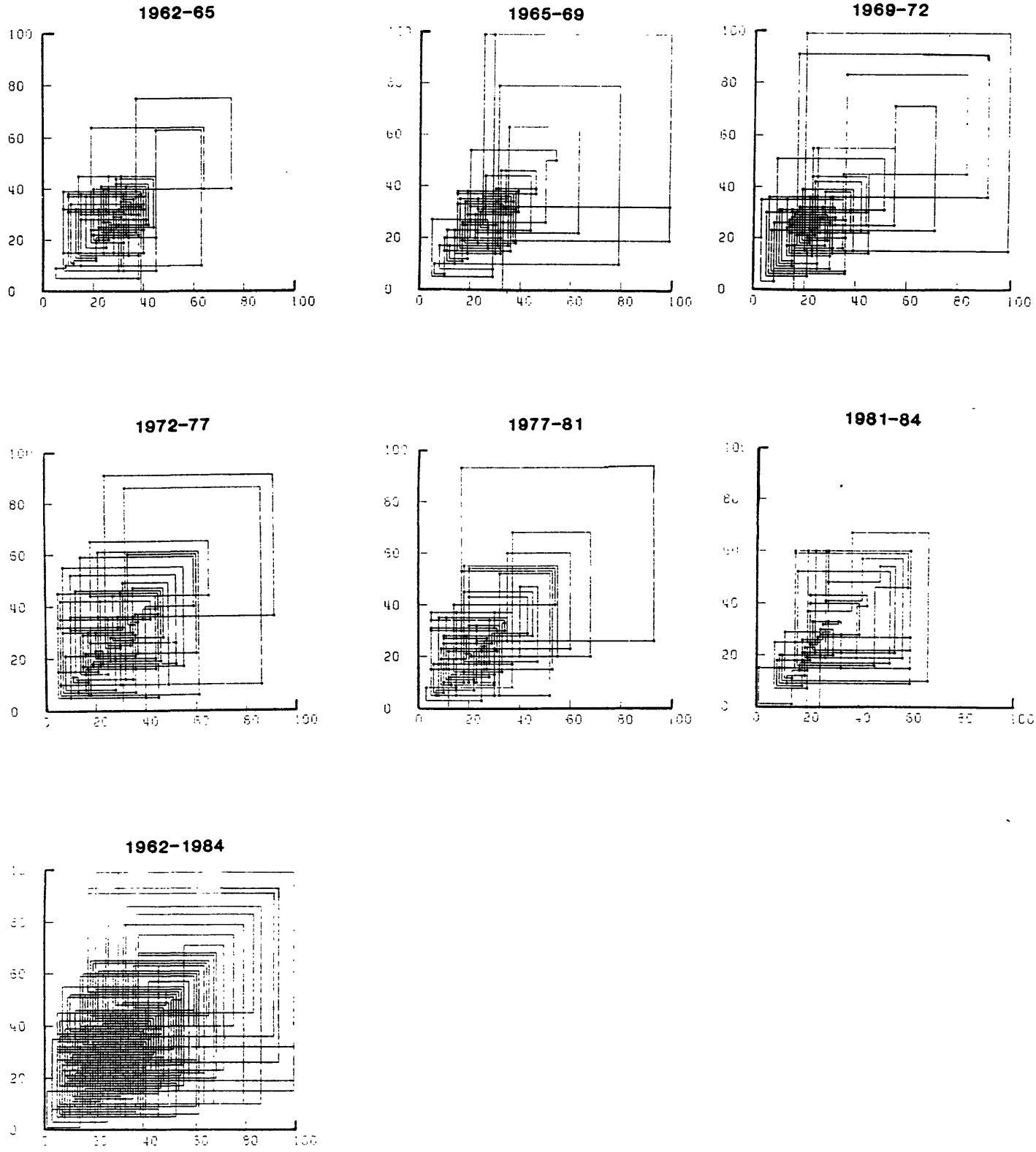

Fig. 6A.

Figure 6. Phase portraits (return maps) of deep tremor based on data of Figure 1 (subdivided into six parts of about same numbers of recurrences, and total for 22 years): dots give one reading *vs.* next reading plotted in sequence of Figure 2; solid lines connect sequences of readings, as in return maps of quadratic equations (*e.g.*, Feigenbaum, 1980) and sine circle map (*e.g.*, Jensen *et al.*, 1984, Fig. 1). Clustering of points on the plane x_{n+1} *vs.* x_n is analogous to clusters on the circle map, *i.e.*, circle map is analog of Poincaré section of portrait of coupled oscillator (see Fig. 5; Fig. 16*D*, panel b):
B. Logarithms of onset times (days).

INTERVALS

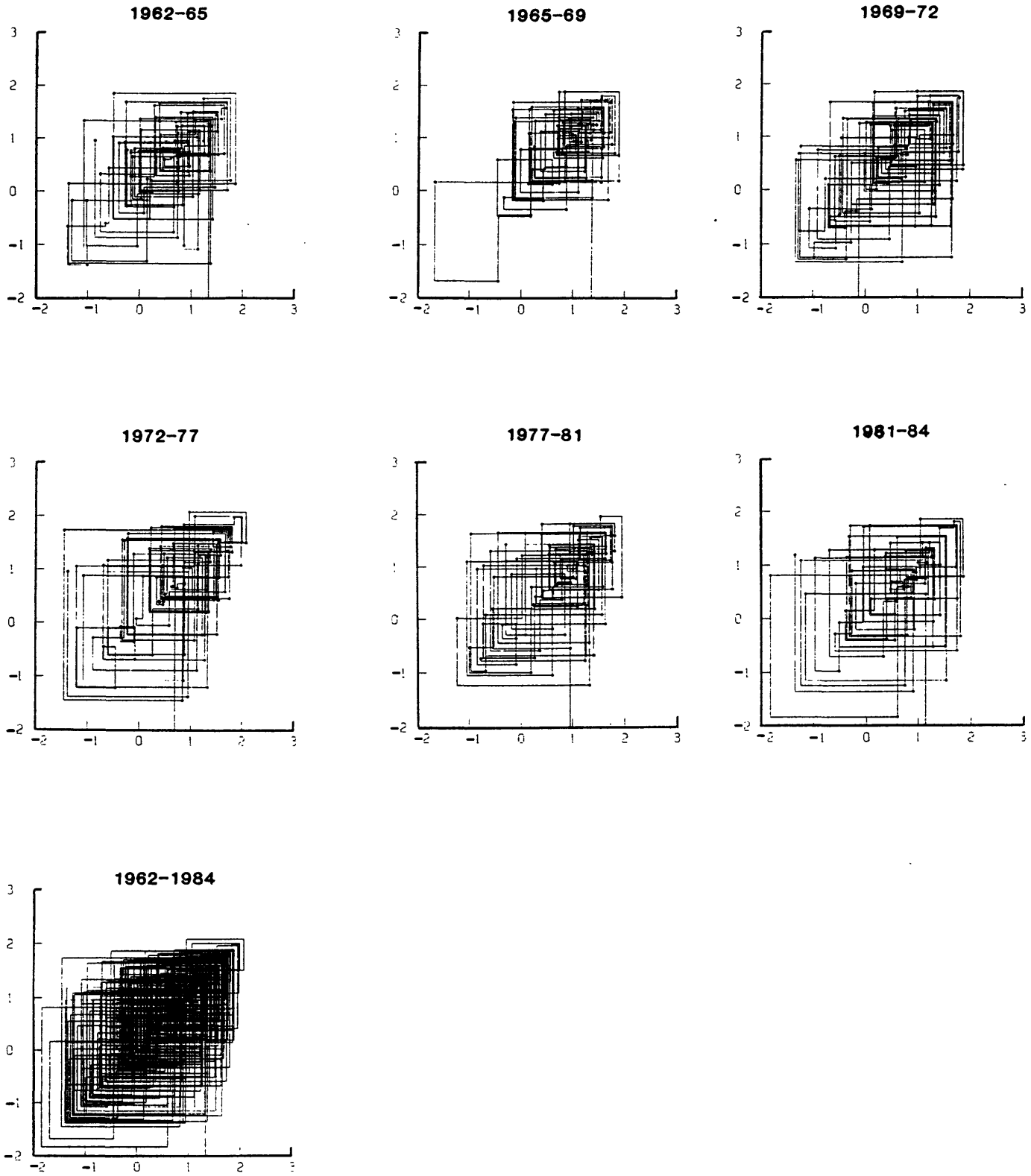

Fig. 6B.

Figure 7. Logarithms of frequencies of occurrences of normalized durations and intervals of tremor episodes (data of Figure 2). Open squares connected by lines are logarithms of count of duration and onset interval per log increment on abscissa; open circles are logarithms of cumulative frequency (number of counts for size $\geq \log X$ on abscissa). Slopes, s, define fractal dimensions, $D = -s$ (derivative of cumulative curves; regressions of incremental values for $\log X$ greater than about -1): (a) Deep durations; bin = 0.04 log unit, 578 counts. (b) Deep onset intervals; bin = 0.08 log unit, 577 counts. (c) Intermediate-depth durations; bin = 0.04 log unit, 347 counts. (d) Intermediate-depth onset intervals; bin = 0.10 log unit, 346 counts.

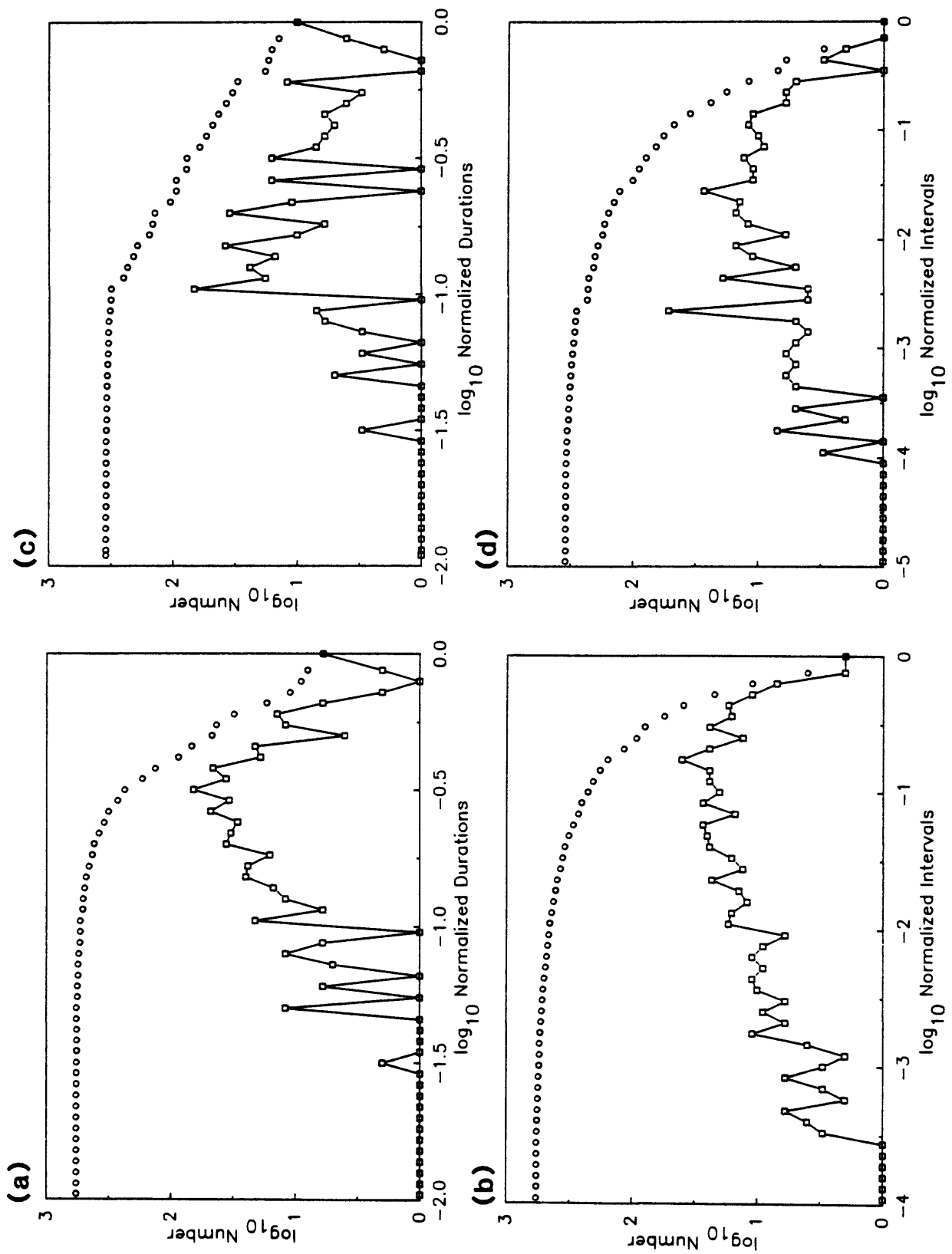
(a)
(b)
(c)
(d)
log10 Number
log10 Normalized Durations
log10 Normalized Intervals

Fig. 7.

Figure 8. Divergence diagrams of return maps of tremor and of logistic equation, $x_{n+1} = 4\lambda x_n(1 - x_n)$. Time sequences as in Figure 2, and equal number of iterations of logistic equation (after transients). Ordinate is running sum $\sum_0^N \Delta x = \sum_0^N (x_{n+1} - x_n)$ (Fig. 6 expressed as fractions of unit range); zero baseline is artifact of starting value. Highest peaks (maximum divergence) represent asymmetry of tremor plots caused by largest excursions relative to average. Periodic attractors have constant repeat interval of constant amplitude (see text): (a) Deep tremor durations; (b) Deep tremor onset intervals; (c) Fixed-point (4-fold) period of logistic equation ($\lambda = 0.880$); (d) Chaotic regime of logistic equation with 4-fold bands ($\lambda = 0.990$); (e) Chaotic regime with 3-fold band and intermittency ($\lambda = 0.970$); (f) Chaotic regime lacking periodic intervals ($\lambda = 0.999$).

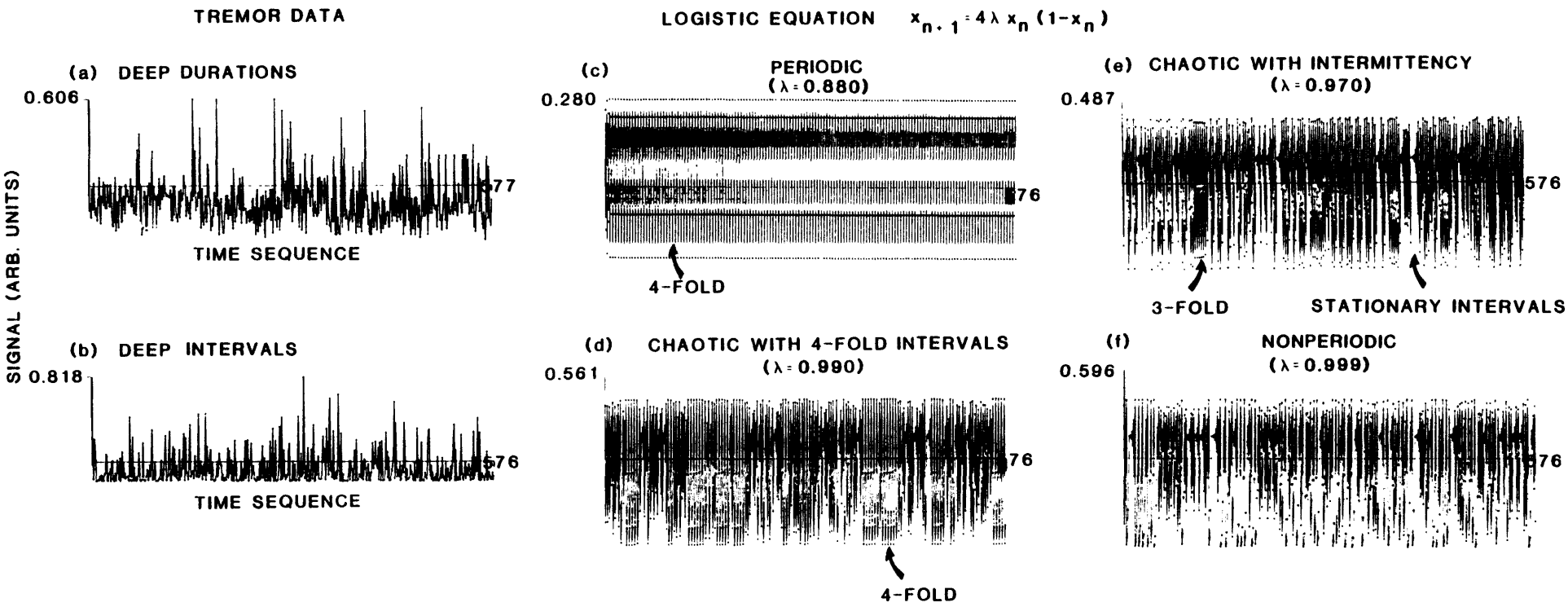
TREMOR DATA
LOGISTIC EQUATION $x_{n+1} = 4\lambda x_n (1-x_n)$
(a) DEEP DURATIONS
0.606
577
TIME SEQUENCE
(b) DEEP INTERVALS
0.818
576
TIME SEQUENCE
SIGNAL (ARB. UNITS)
(c) PERIODIC
(λ = 0.880)
0.280
576
4-FOLD
(d) CHAOTIC WITH 4-FOLD INTERVALS
(λ = 0.990)
0.561
576
4-FOLD
(e) CHAOTIC WITH INTERMITTENCY
(λ = 0.970)
0.487
576
3-FOLD
STATIONARY INTERVALS
(f) NONPERIODIC
(λ = 0.999)
0.596
576

Fig. 8.

Figure 9. Test for period-doubling in tremor data: A. Histogram of counts of deep tremor durations illustrating average spacing, d_{avg} ($\approx \bar{d}$), at given count frequency, representing average 'period,' N, of spacing in return map (see Fig. 6A); $\bar{d}_n$ is average spacing between branches of specific bifurcation pairs (solid bars in 9C) at fixed λ, and d_{avg} is average spacing between entire set of N branches (solid + dashed bars in 9C). B. Logarithm of d_{avg} *vs.* $\log N$ from A compared with measure in period-doubling attractor (bifurcations of tree in C). Theoretical packing ratio, $\nu = \bar{d}_n/\bar{d}_{n+1}$, for period-doubling attractor is 2.5029... (universality parameter of Feigenbaum, 1978, 1980); corresponding slope ≈ -1.32. C. Example of $d_{\mathrm{avg}} \approx \bar{d}_{n+1}$ for $N = 4$ in period-doubling bifurcation diagram (from Testa *et al.*, 1982); return map analogous to Fig. 6 is constructed by plotting x-values over variable range of λ (λ_1, λ_2, λ_3 mark successive doublings; $\lambda_{\mathrm{critical}}$ marks transition to chaos). Fine structure of chaotic regime (periodic windows, crises, etc.) illustrated by Jeffries (1985), Jensen (1987, Fig. 3).

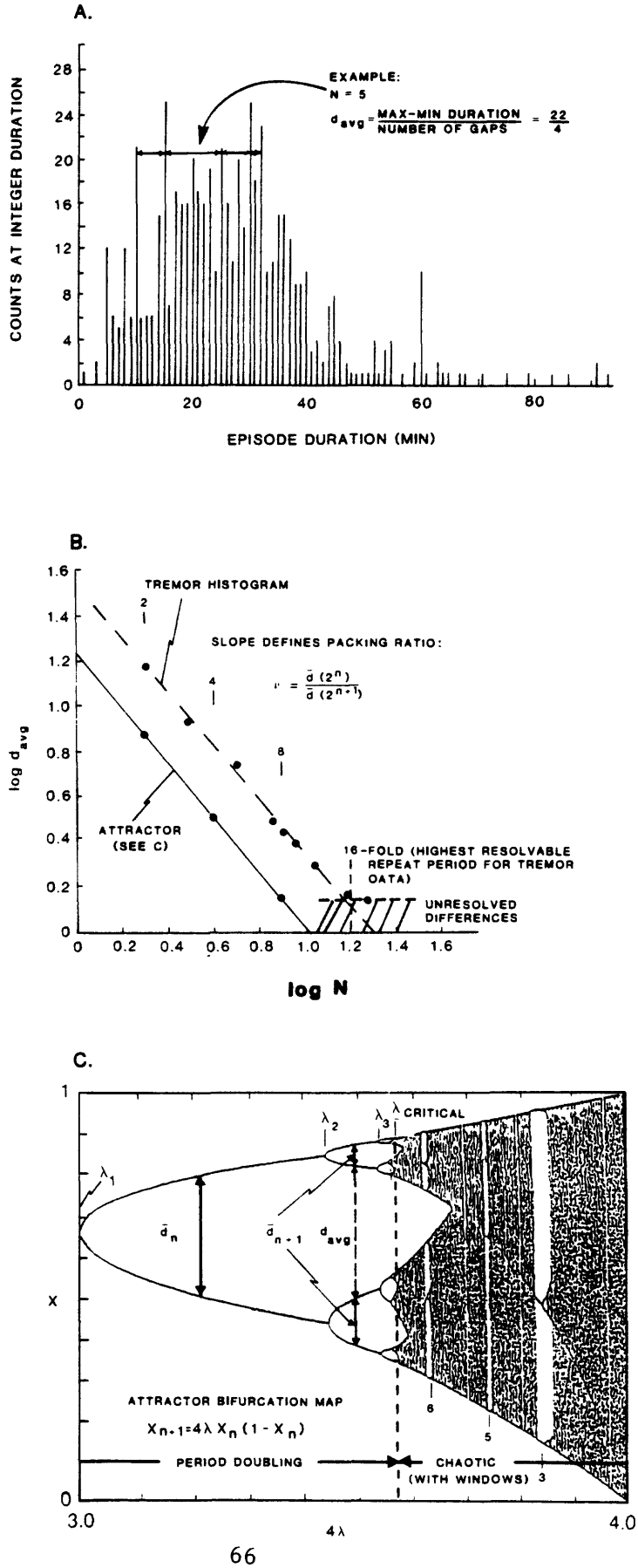
A.
COUNTS AT INTEGER DURATION
EPISODE DURATION (MIN)
EXAMPLE:
N = 5
$d_{avg} = \frac{\text{MAX-MIN DURATION}}{\text{NUMBER OF GAPS}} = \frac{22}{4}$
B.
log d_{avg}
log N
TREMOR HISTOGRAM
SLOPE DEFINES PACKING RATIO:
$\nu = \frac{\bar{d}(2^n)}{\bar{d}(2^{n+1})}$
ATTRACTOR (SEE C)
16-FOLD (HIGHEST RESOLVABLE REPEAT PERIOD FOR TREMOR DATA)
UNRESOLVED DIFFERENCES
C.
CRITICAL
ATTRACTOR BIFURCATION MAP
$X_{n+1} = 4\lambda X_n (1 - X_n)$
PERIOD DOUBLING
CHAOTIC (WITH WINDOWS)
X
4λ

Fig. 9.

Figure 10. Fourier transform analyses of tremor data for tremor rates of Fig. 4 (left) and divergence series of Fig. 8 (right): (a) Deep tremor rates; sample size = 8192 (2^n nearest 8030 days in Fig. 4), frequency increment = 1.2207×10^{-4} cycle/day, max. frequency 0.50 cycle/day. Spectrum meaningful for periods above 5 days (frequencies below 0.2 cycle/day); evidence of unique period is weak peak at 5.33×10^{-3} cycle/day (188 days). (b) Intermediate-depth tremor rates, analyzed as in (a); no indication of unique periods. (c) Event series of deep tremor durations of Figure 8(a); sample size = 1024 (2^n nearest 577 events), no evidence of special recurrence intervals (see discussion of Fig. 8). (d) Event series of deep tremor onset intervals of Figure 8(b) analyzed as in (c).

(a)
(b)
(c)
(d)
LOG10 (AMPLITUDE SPECTRAL DENSITY, MIN.)
FREQUENCY (CYCLE/DAY)
PERIOD (DAY)
SIGNAL (ARB. UNITS)
FREQUENCY (ARB. UNITS)

Fig. 10.

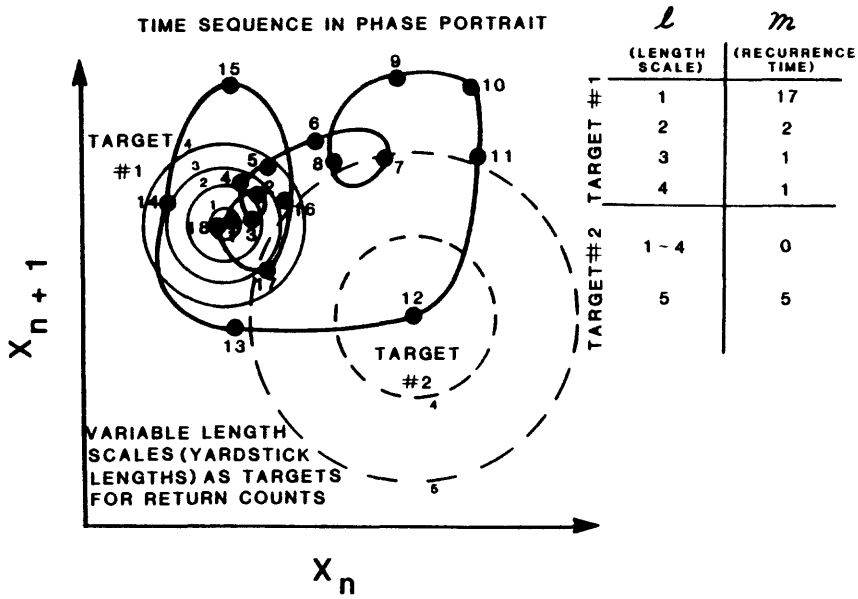

Figure 11. Schematic return map illustrating enumeration of recurrence times, m_i, defined as number of steps (iterations) in phase space that occur between one visit and the next visit within a phase-space piece, or target, of diameter ℓ_i (see text for partitioning over entire space). Steps are numbered 1 through 18. Two targets are shown, one centered near step 1 (solid circles), the other at step 12 (dashed). Numbers on circles are values of ℓ (arbitrary scale); number of steps (m_i) between "hits" within target ℓ listed at right.

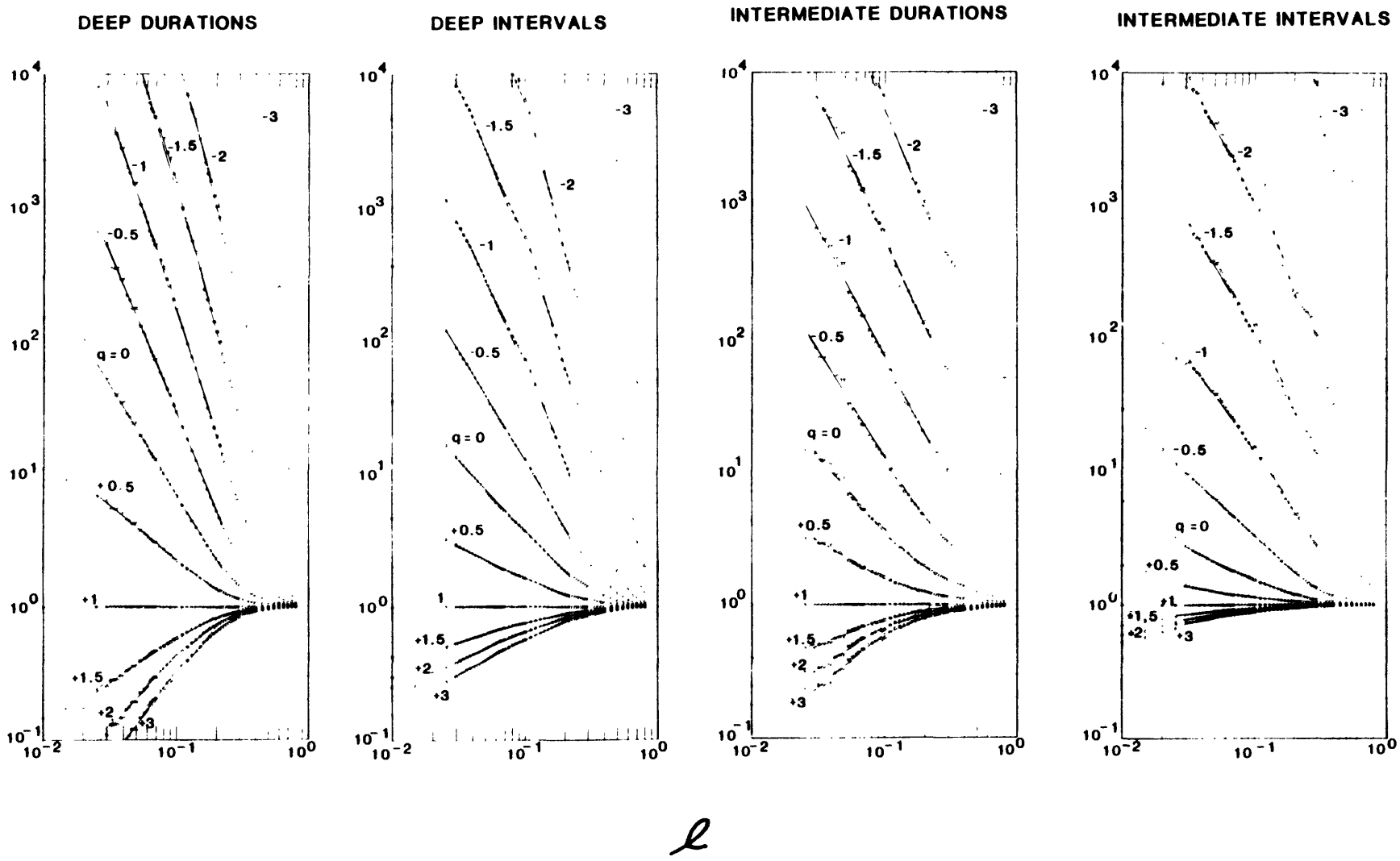

Figure 12. Plots of expanded recurrence times, $\langle m^{1-q} \rangle$ *vs.* target length, ℓ, for each set of tremor data in Fig. 6. Straight line segments are regressions of slopes τ over selected intervals (*cf.*, Fig. 13*A*; see Eqs. (6) and (10)).

Figure 13. Relationships between τ, q, α, and $f(\alpha)$ (see definitions in text): A. Apparent τ (τ_a) based on average slopes intersecting $\log \ell = 0$ (see Eq. (6)). B. τ_a from data of circle map in Fig. 15*A* for three values of $\log \ell$ (-1.0, -1.4, -2.0) (symbols) and ranges of product $q\alpha$ (vertical bars). $f(\alpha)$ is difference $q\alpha - \tau_a$ (Eq. (8)); negative values not physical (see error bars, Fig. 15*B*). C. Schematic of B for well-behaved data; product $q\alpha$ (upper solid curve) and τ (lower solid curve) define $f(\alpha)$ envelope (stippled region); $f(\alpha)$ at q indicated by vertical lines. For uniform distribution in phase space (random set), $\alpha = d\tau/dq = 1$ and $\alpha = f(\alpha) = 1$ (constant differences shown by dashed lines; see text and Fig. 16*F*).

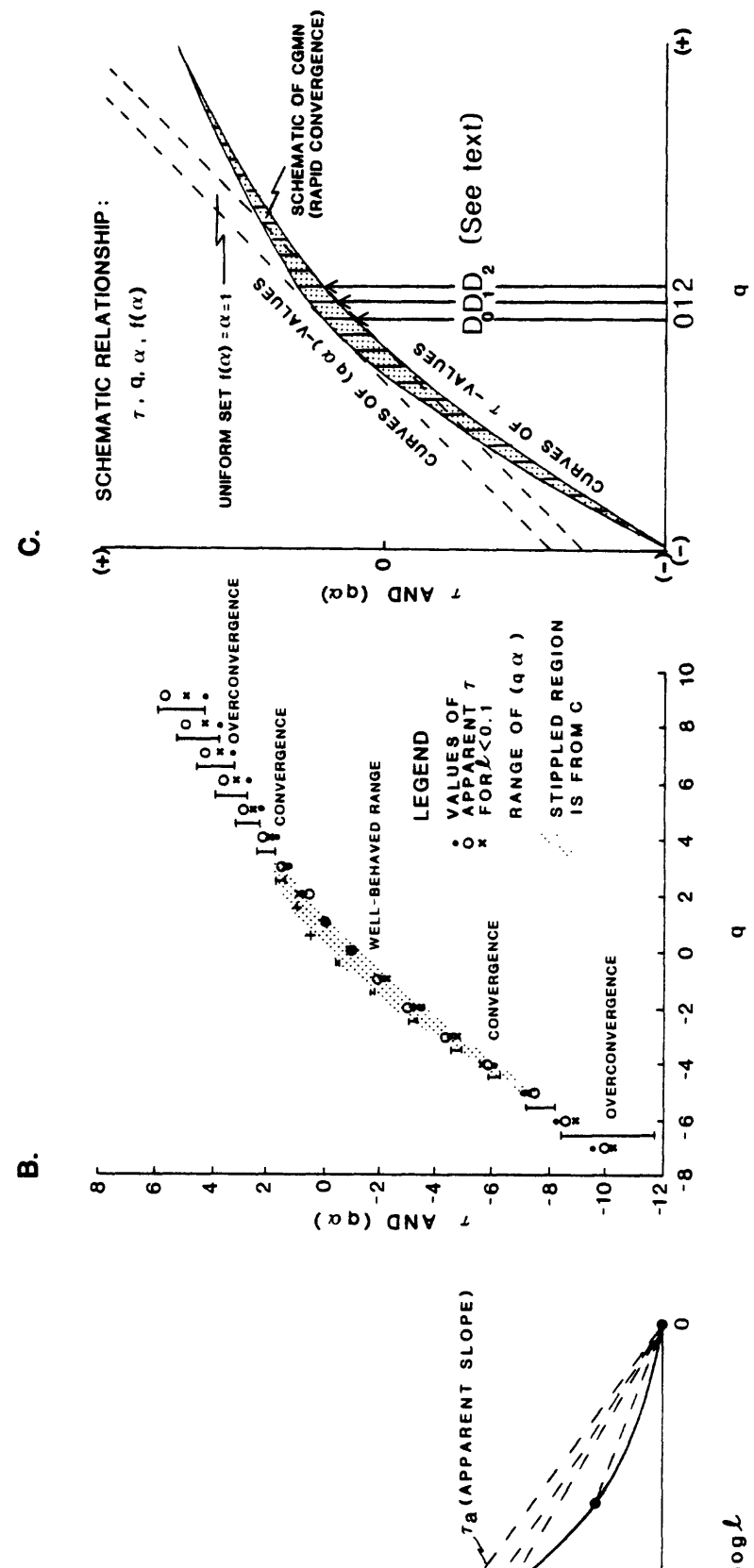
A.
B.
C.
SCHEMATIC RELATIONSHIP:
τ, q, α, f(α)
UNIFORM SET f(α) = α = 1
SCHEMATIC OF CGMN (RAPID CONVERGENCE)
CURVES OF (qα)-VALUES
CURVES OF τ-VALUES
(See text)
τ AND (qα)
q
LEGEND
VALUES OF APPARENT τ FOR ℓ<0.1
RANGE OF (qα)
STIPPLED REGION IS FROM C
WELL-BEHAVED RANGE
CONVERGENCE
OVERCONVERGENCE
τa (APPARENT SLOPE)
log ℓ

Fig. 13.

Figure 14. Singularity spectra for return maps of tremor constructed from normalized data of Figure 2 and method of Fig. 13 for $\log \ell = -1$ (crosses), $\log \ell = -2$ (dots) and their averages (open circles) for values of q from -7 to +12 (*cf.*, Fig. 12). Solid lines are CGMN reference curve of Halsey *et al.* (1986, Fig. 14); see Fig. 16*D*. Negative values of $f(\alpha)$ explained in Fig. 13*B*: (a) Deep durations (577 points in portrait). (b) Deep tremor intervals (576 points). (c) Intermediate-depth durations (346 points). (d) Intermediate-depth intervals (345 points).

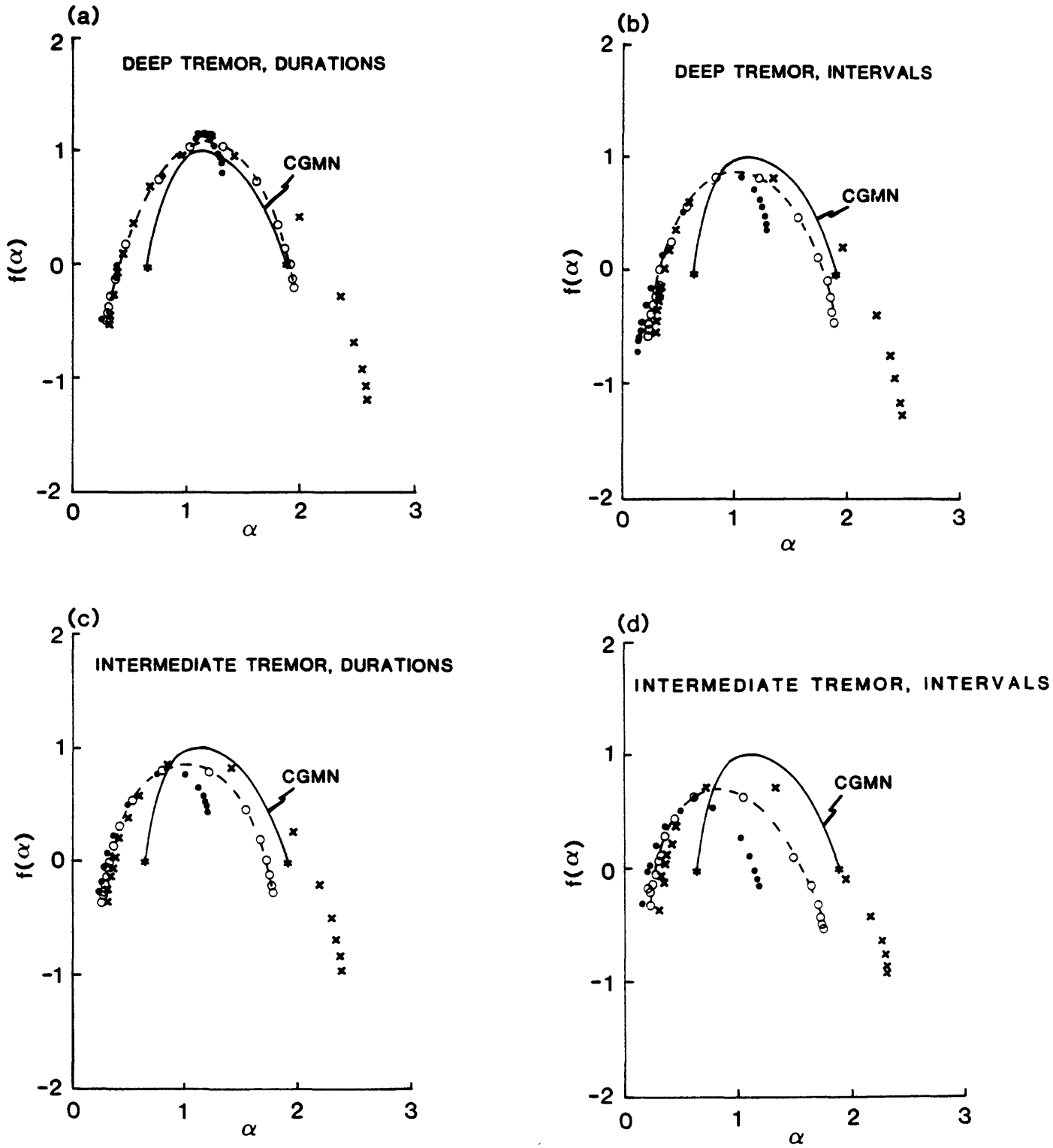
(a)
DEEP TREMOR, DURATIONS
CGMN
f(α)
α
(b)
DEEP TREMOR, INTERVALS
CGMN
f(α)
α
(c)
INTERMEDIATE TREMOR, DURATIONS
CGMN
f(α)
α
(d)
INTERMEDIATE TREMOR, INTERVALS
CGMN
f(α)
α

Fig. 14.

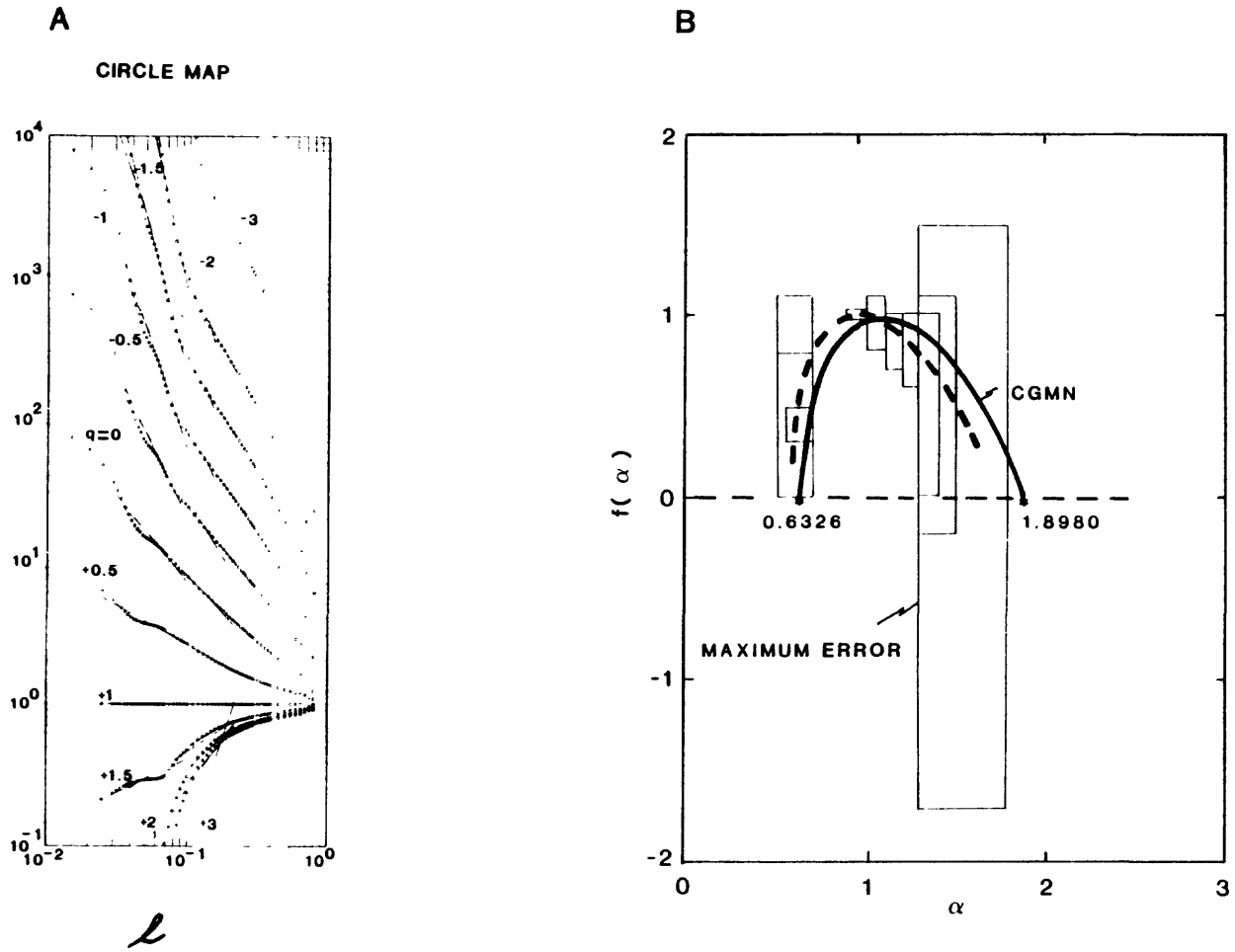

Figure 15. Recurrence times $\langle m^{1-q} \rangle$ *vs.* ℓ and singularity spectrum calculated for reference set of 600 data points in circle map of Eq. (13) for $\Omega = 0.61 \pm 0.01$ and $K = 1$. A Recurrence times expanded *vs.* q as in Fig. 12. B Values of α *vs.* $f(\alpha)$ evaluated as in Fig. 13*B*, illustrating propagation of errors (boxes) and averages (dashed) near reference curve (solid) of Halsey *et al.* (1986, Fig. 14). The CGMN curve (solid) corresponds to $W_g = (5^{1/2} - 1)/2 \approx 0.618034\ldots$ in Eq. (14) and range of Ω near 0.6066 in Eq. (13) (latter by trial and error bracket of W_g). Theoretical limits are $\alpha_{\min} = 0.6326\ldots$ and $\alpha_{\max} = 1.8980\ldots$ at $f(\alpha) = 0$, and $f(\alpha)_{\max} = 1$ (exactly). Negative errors in $f(\alpha)$ explained in Fig. 13*B*.

Figure 16. Examples of spectra for different measures. Maxima of $f(\alpha)$ are Hausdorff dimension, D_0; $f(\alpha) = 0$ defines limits of probability densities ($\alpha_{\min}$ is singularity strength of most dense and $\alpha_{\max}$ of most rarefied measures; *e.g.*, panel c in B): A. Two-scale Cantor set: (a) Singularity spectrum. (b) Recurrence ratios. (c) Standard Cantor set; spectrum degenerates to $f(\alpha) = \alpha = 0.6309\ldots$ (asterisk in (a)) (from Halsey *et al.* , 1986, Figs. 1, 2, and 4). B. Period-doubling set: (a) Singularity spectrum (from Halsey *et al.* , 1986, Fig. 9). (b) Recurrence relations (from Halsey *et al.* , 1986, Fig. 7). (c) Bifurcation diagram (forcing increases downward) analogous to Fig. 9C (dense regions are mixed odd-period, period-doubling, and aperiodic sets of chaotic regime; from Jeffries , 1985, Fig. 2). C. Mode-locked sets of sine circle map: (a) Singularity spectrum. (b) Devil's staircase of rational winding numbers (Eq. 14) (from Halsey *et al.* , 1986, Figs. 10 and 12); *cf.*, Bak (1986), Shaw (1987b). D. Critical transition of circle map (CGMN): (a) Singularity spectrum; see parameters in Fig. 15*B* (from Halsey *et al.* , 1986, Fig. 14). (b) Poincaré section of coupled oscillatory convection tuned to CGMN condition (points are temperature readings; from Jensen *et al.* , 1985, Fig. 1). E. Schematic of truncated singularity spectrum for $f(\alpha)_{\max} = 1$ and arbitrary α (from Halsey *et al.* , 1986, Fig. 5). F. Degenerate set representing nonsingular (uniform) background $f(\alpha) = \alpha = 1$ interrupted by singularities of arbitrary discrete set with fixed α and $f(\alpha)$. Set plots at points (1,1) and ($\tilde{\alpha}$, $\tilde{f}(\alpha)$) in the spectrum (from Halsey *et al.* , 1986, Fig. 6).

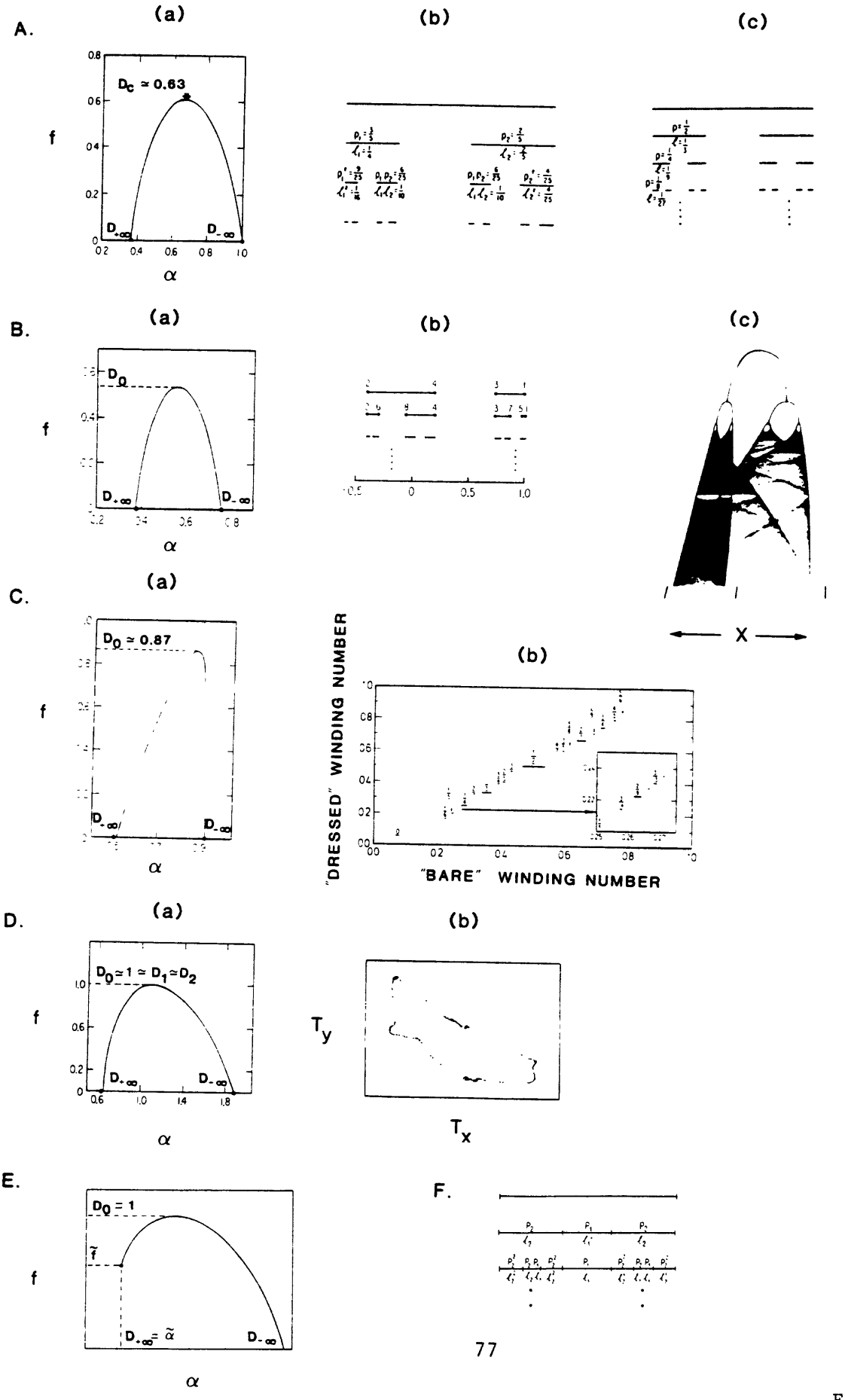
A.
(a)
(b)
(c)
f
$D_c \simeq 0.63$
$D_{+\infty}$
$D_{-\infty}$
α
B.
(a)
(b)
(c)
f
D_0
$D_{+\infty}$
$D_{-\infty}$
α
X
C.
(a)
(b)
f
$D_0 \simeq 0.87$
$D_{+\infty}$
$D_{-\infty}$
α
"DRESSED" WINDING NUMBER
"BARE" WINDING NUMBER
D.
(a)
(b)
f
$D_0 \simeq 1 \simeq D_1 \simeq D_2$
$D_{+\infty}$
$D_{-\infty}$
α
T_y
T_x
E.
F.
f
$D_0 = 1$
$\tilde{f}$
$D_{+\infty} = \tilde{\alpha}$
$D_{-\infty}$
α

Fig. 16.

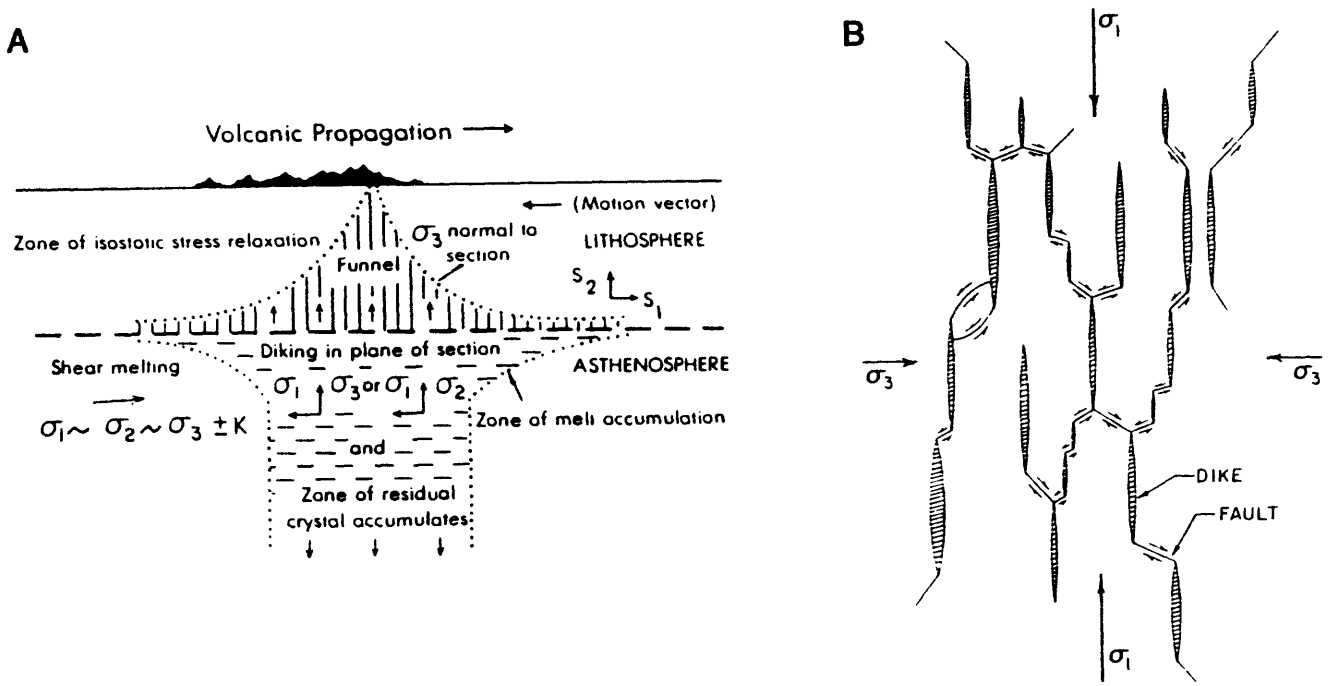

Figure 17. Schematic illustration of magma transport path from source to surface, from Shaw (1980, Figs. 5 and 11): A. Longitudinal section of edifice, crust, lithosphere, and asthenosphere showing inferred stress distributions and convergent path of magma rise. B. Idealization of fluid-filled cracks distributed in dendritic clusters of self-similar fractal sets in vertical and horizontal sections; crack shapes and connectivities (after Hill, 1977) symbolize regimes ranging from pure extension (shaded) to pure shear (solid lines with arrows) according to failure regimes in Shaw (1980). See text for dike measurements and fractal dimensions.